



HAL
open science

Synthesis of piliostigma reticulatum decorated TiO₂ based composite and its application towards Cr(VI) adsorption and bromophenol blue degradation: Nonlinear kinetics, equilibrium modelling and optimisation photocatalytic parameters

Sali Mouhamadou, Sadou Dalhatou, David Obada, Lydia Fryda, Angélique Mahieu, Pierre Bonnet, Christophe Caperaa, Abdoulaye Kane, Harouna Massai, Hicham Zeghioud

► To cite this version:

Sali Mouhamadou, Sadou Dalhatou, David Obada, Lydia Fryda, Angélique Mahieu, et al.. Synthesis of piliostigma reticulatum decorated TiO₂ based composite and its application towards Cr(VI) adsorption and bromophenol blue degradation: Nonlinear kinetics, equilibrium modelling and optimisation photocatalytic parameters. Journal of Environmental Chemical Engineering, 2023, 11 (1), pp.109273. 10.1016/j.jece.2023.109273 . hal-04027928

HAL Id: hal-04027928

<https://normandie-univ.hal.science/hal-04027928v1>

Submitted on 8 Jan 2025

HAL is a multi-disciplinary open access archive for the deposit and dissemination of scientific research documents, whether they are published or not. The documents may come from teaching and research institutions in France or abroad, or from public or private research centers.

L'archive ouverte pluridisciplinaire **HAL**, est destinée au dépôt et à la diffusion de documents scientifiques de niveau recherche, publiés ou non, émanant des établissements d'enseignement et de recherche français ou étrangers, des laboratoires publics ou privés.



Distributed under a Creative Commons Attribution - NonCommercial 4.0 International License

1 **Synthesis of piliostigma reticulatum decorated TiO₂ based composite and its**
2 **application towards Cr(VI) adsorption and bromophenol blue degradation:**
3 **Nonlinear kinetics, equilibrium modelling and optimisation photocatalytic**
4 **parameters**

5 Sali Mouhamadou^{a,b}, Sadou Dalhatou^{b,*}, David O. Obada^{c,f}, Lydia Fryda^a, Angélique
6 Mahieu^a, Pierre Bonnet^d, Christophe Caperaa^d, Abdoulaye Kane^a, Harouna Massai^e,
7 Hicham Zeghioud^{a,*}

8 ^aUniLaSalle-École des Métiers de l'Environnement (UniLaSalle-EME), Cyclann,
9 Rennes, 35170 Bruz, France

10 ^bDepartment of Chemistry, Faculty of Science, University of Maroua, 814 Maroua,
11 Cameroon

12 ^cMultifunctional Materials Laboratory, Department of Mechanical Engineering,
13 Ahmadu Bello University, 810222 Zaria, Nigeria

14 ^dInstitut de Chimie de Clermont-Ferrand, Université Clermont Auvergne, UMR 6296,
15 BP 10448, F-63000 Clermont-Ferrand, France

16 ^eDepartment of Chemistry, Chemical Engineering & Mineral Industries School,
17 University of Ngaoundéré, Cameroon

18 ^fAfrica Centre of Excellence on New Pedagogies in Engineering Education, Ahmadu
19 Bello University, 81022, Zaria, Nigeria

20

21 *Corresponding authors: hicham.zeghioud@unilasalle.fr Tel: +33636084296 ;
22 dalsaous@yahoo.fr

23 **Abstract**

24 In this study, the use of wild bio-waste piliostigma fruits as an alternative precursor
25 for titanium dioxide doped carbon and a simple synthesis method for the preparation
26 of novel eco-friendly TiO₂-AC (AC stand for activated carbon) based composites
27 following two routes (TiO₂-AC₁ and TiO₂-AC₂) were proposed. The structure,
28 morphology, chemical composition, surface area, light absorption and crystalline
29 phase of the composites were systematically characterised using Fourier transform
30 infrared spectroscopy, scanning electron microscopy, BET analysis, Raman
31 spectroscopy, X-ray fluorescence spectrophotometry fundamental parameters and X-
32 ray Diffraction. The adsorptive capability of the composites were tested towards
33 Cr(VI) elimination and the Box Behnken Design (BBD) with a desirability function was

34 implemented to optimise the photocatalytic parameters towards Bromophenol Blue
35 (BPB) dye degradation. As a result, high adsorption quantity of 3.46 mg/g (TiO₂-AC₁)
36 and 3.49 mg/g (TiO₂-AC₂) were obtained at optimum adsorption parameters. Kinetics
37 study showed a good nonlinear fit with pseudo second order and isotherms
38 modelling are well described by Sips and Marczewski-Jaroniec models. The
39 degradation efficiency of bromophenol blue (BPB) by the TiO₂-AC₂ composite
40 reached 100%, however 57.90% only was recorded for TiO₂ at about 180min of UV
41 irradiation. The kinetics of degradation followed pseudo first order model and the
42 optimal conditions provided by the response surface methodology (RSM) was pH 3,
43 photocatalyst dose 300mg/L and salt interference of 10mg/L. This trend proposed a
44 mechanism for preparation of biomass-based TiO₂-AC composite and revealed that
45 the use of RSM optimisation process contributes to save time and ensure proper
46 materials handling through degradation as a sustainable water treatment technology.

47 **Keywords:** Photocatalysis, Box Behnken Design, Cr(VI), bromophenol blue,
48 optimisation, Adsorption

49 1. Introduction

50 Water contamination is a global concern and a huge environmental issue that
51 necessitates researchers from numerous areas to collaborate towards sustainable
52 solutions. Controlling water xenobiotics in the ecosystems is a serious concern all
53 around the world. One of the main causes of water pollution is industrial waste, which
54 has a negative impact on the environment [1]. Organic dyes are organic pollutants
55 that represent effective chemical hazard encountered in our environment [2]. About
56 1.6 million tons of dyes are being manufactured annually, 10-15% of which are being
57 discarded in the form of unprocessed wastewater effluent into the aquatic systems
58 [3]; [4]. Bromophenol blue (BPB), is a non-biodegradable synthetic hazardous dye
59 which has wide applications as colour marker in labs, as acid-base indicator and for
60 agarose gel electrophoresis; along with applications in drug, cosmetics, textile and
61 printing ink industries [5]. Bromophenols have shown serious impact on the
62 ecosystem due to their genotoxic, mutagenic and carcinogenic properties [6].
63 Relevant research investigation have focused on the removal of dyes such as
64 methylene blue, Congo red [7], crystal violet [8], methyl orange, rhodamine B [9] and
65 direct red 80 [10], with only a few reports on bromophenol blue [7]. Bromophenol blue
66 , a widely used dye, can easily migrate through aquifers and generate widespread

67 pollution of surface waters due to high solubility [11]. On the other hand, heavy
68 metals contamination are no doubt one of the biggest environmental threats today
69 [12]. Chromium is a metal ion employed in various sectors. It includes textile,
70 metallurgies, tanning, electroplating and colouring [13], wood preservation and
71 industrial pigmentation [14]. This inorganic metal mostly exists in two valence states
72 which are trivalent chromium Cr(III) and hexavalent chromium Cr(VI). While Cr(III) is
73 considered non-toxic, Cr(VI) is toxic, causing serious health problems to humans
74 [15]. The maximum allowable limit recommended by the World Health Organisation
75 (WHO) for Cr(VI) is 0.05 mg.L^{-1} [13]. Excessive intake of Cr(VI) can lead to cancers,
76 nervous system failure, and kidney damage [16]. Therefore, the treatment of
77 industrial wastewater containing the BPB dye and the toxic Cr(VI) is of paramount
78 importance to limit their harmful impacts, even more if their elimination is achieved
79 through a simple and eco-friendly process that should be given significant attention.

80 The treatment of wastewater have been done using various physicochemical
81 methods such as coagulation, chemical oxidation [17], photodegradation,
82 nanofiltration [18], bioremediation, flocculation, ozonation [19], photocatalysis [20,21]
83 and adsorption [22–24]. However, most of these processes are capital intensive,
84 complicated and require considerable quantities of chemicals. The adsorption of
85 pollutants like Cr(VI) onto bio-based materials is a process with certain advantages,
86 due to its simplicity, low cost, effectiveness, biodegradability and reusability [7]; [25].
87 Photocatalysis, known better as advanced oxidation process (AOP) which is the most
88 suitable method to oxidise organic xenobiotic such as BPB extensively and non-
89 selective. It's also a quick and low cost approach design to eliminate both cationic
90 and anionic dyes [26], and facilitate heavy metal reduction including hexavalent
91 chromium [27].

92 Numerous materials have been developed and used to improve water quality in
93 recent years. The elimination of both organic and inorganic contaminants of water
94 highly depends on the physicochemical properties of the substrate, including surface
95 area, porous structure and surface functional groups. Considerable efforts have been
96 done in recent decades to create effective and selective adsorbents [15] like
97 activated carbon [28] and non-selective photocatalysts, including TiO_2 Impregnated
98 polyester [29], $\text{Cu}_x\text{O}/\text{TiO}_2$ [30], heat activated $\text{K}_2\text{S}_2\text{O}_8$ [31], chitosan composite of
99 metal-organic framework [32], $\text{ZnO}/\text{graphene oxide nanocomposites}$ [33], Samarium
100 loaded TiO_2 [34] and $\text{ZnO}/\text{Nb}_2\text{O}_5$ catalyst [35] for the elimination of toxic pollutants

101 from water/wastewater. Recently, various types of biomass have been used for the
102 synthesis of new adsorbents and photocatalysts such as rice husk, orange peels,
103 corncob, cotton waste, sugarcane bagasse, just to mention a few [36]. Based on the
104 concept of green chemistry and in the framework of circular economy, agricultural
105 biomass waste are potential candidates for the development of materials with
106 adsorptive properties [37] and photocatalytic efficiency. Among them, *Piliostigma*
107 *reticulatum* fruits from the North region of Cameroon is one of the most important wild
108 solid wastes which represents a potential and eco-friendly biomass that can be use in
109 water treatment technology.

110 To the best of the authors' knowledge, there are no studies on the use of *piliostigma*
111 biomass (resource from Cameroon) for the synthesis of a bifunctional material (TiO_2
112 based composites) to tackle wastewater treatment in Cameroon and their
113 physicochemical characterisation. This study reports for the first time, the
114 characteristics of *piliostigma reticulatum* with its decorated TiO_2 composites
115 synthesised using two routes ($\text{TiO}_2\text{-AC}_1$ and $\text{TiO}_2\text{-AC}_2$) and investigate the adsorption
116 capability of Cr(VI) and photocatalytic optimisation of BPB degradation using Expert
117 design software (UniLaSalle-EME, Rennes, France). The efficacy of the composites
118 for the elimination of water contaminants (organic and inorganic) has been
119 investigated for various key operational parameters such as contact time, adsorbent
120 dose, pH and concentration. Equilibrium modelling of isotherms and kinetics was
121 applied to analyse the adsorption data and to propose adsorption mechanism while
122 the optimisation of three parameters of response surface methodology using Box-
123 Behnken approach, scavenging effect and implication of radicals was implemented
124 for photocatalytic study.

125 **2. Material and Methods**

126 **2.1. Reagents**

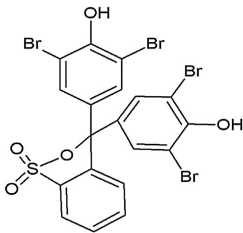
127 The dye solid powder of BPB (pure) was purchased from REACTIFS RAL (Paris,
128 France). The general characteristics and structure of BPB are presented in Table 1.
129 A stock solution of 500 mg/L was prepared using 0.5 g in 1 L of osmotic water and
130 the solutions with the desired concentrations were obtained via dilution process.
131 Potassium dichromate ($\text{K}_2\text{Cr}_2\text{O}_7$ 99.5%, Panreac Quimiga) stock solution of 100 mg/L
132 were used for further experiments. HCl (37%, Fluka, Austria), and NaOH (97%,
133 sigma Aldrich, India) diluted solutions were used to adjust the pH values. Methanol

134 (99.8%, Merck, Germany), isopropanol (99%, Merck, Germany), Titanium (VI)
 135 isopropoxide (98%+, Acros Organics, China), sulphuric acid (Fischer Scientific,
 136 USA), 1.5-diphenylcarbazine (sigma Aldrich) and Phosphoric Acid (85%, Carlo Erba
 137 Reagent, France) were used for others experiments. All chemicals were of analytical
 138 grade and used without any further purification. The BPB solution have a natural pH
 139 of 4.35 while the one Cr(VI) solution is 4.76.

140

141

Table 1 Chemical characteristics and structure of BPB dye

Characteristic	Bromophenol Blue (BPB)
Molecular Structure	
Chemical formula	C ₁₉ H ₁₀ Br ₄ O ₅ S
Molecular weight (g/mol)	669.96
λ_{\max} (nm)	592

142

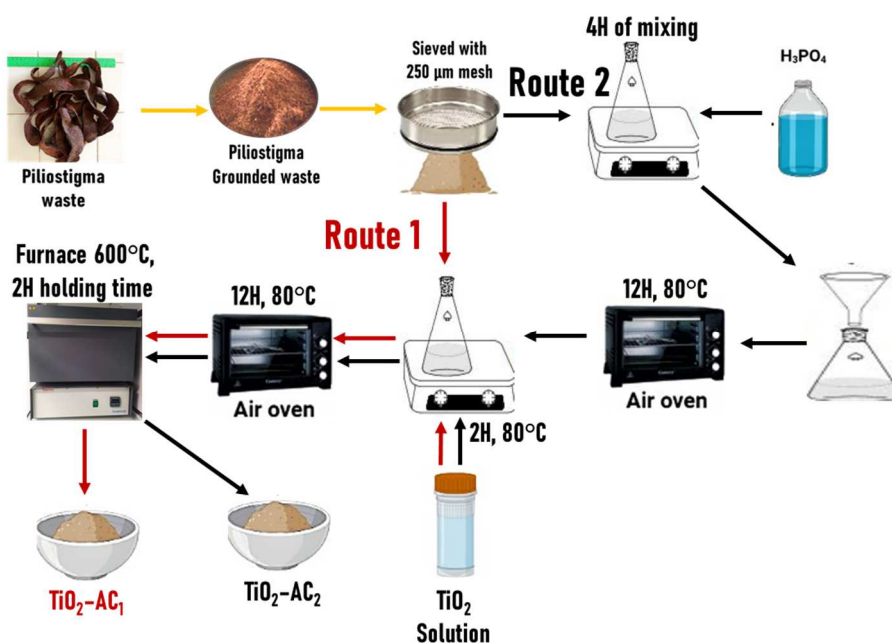
143 **2.2. Synthesis of pristine piliostigma biomass (PBS) and composites-based** 144 **materials**

145 **2.2.1. Preparation of piliostigma biomass (PBS) and activated PBS**

146 The biomaterial (piliostigma fruits) used in the present study is a popular shrub of the
 147 family Caesalpinia that can be found throughout Sahel Africa in countries such as
 148 Cameroon, Senegal and Sudan. The fruits were collected from Pont palais hills,
 149 Mayo-Oulo, North region of Cameroon. They were thoroughly cleaned with distilled
 150 water and dried in air oven at 105°C for 24 h. The dry fruits were crushed using a
 151 grinder and sieved to get particles less than 315 μm . The obtained biomass (PBS)
 152 was used for characterisation and composites synthesis. 50 g of activated PBS was
 153 produced by treating the obtained biomass with phosphoric acid 2 M in the ratio of
 154 1:5(w/v) followed by incubation at 80 °C in a hot air oven for 12 hours.

155 **2.2.2. *Piliostigma reticulatum* decorated TiO₂ based composites synthesis**

156 Sol-gel is one of the most applied processes to support catalysts in biomass-based
157 materials. *Piliostigma* decorated TiO₂ based composites were synthesised following
158 two synthetic routes summarised in scheme A. Initially, TiO₂ solution was prepared
159 using Titanium (VI) isopropoxide (TTIP) precursor and hydrochloride acid. In brief,
160 100 mL of TTIP was introduced in 500 mL Erlenmeyer and 150 mL of HCl (9 M) was
161 added under stirring for 30 minutes. 250 mL of osmotic water was then added to the
162 mixture and let for maturation time (4 hours) at ambient temperature. For composites
163 synthesis, pristine PBS (for TiO₂-AC₁) or activated PBS (for TiO₂-AC₂) (20 g) were
164 added to 100 mL of TiO₂ solution and the mixture was magnetically stirred for 2 hours
165 at 80 °C. The resulting TiO₂ based composites was transferred to an oven and was
166 dried at 80 °C for 12 hours. The dried composites were calcinated in a
167 THERMOLYNE muffle furnace (ThermoSCIENTIFIC) at 600 °C for 2 hours in air and
168 cooled at room temperature (25 °C). The resulted products named TiO₂-AC₁ and
169 TiO₂-AC₂ composites were grounded with mortar and then saved in sealed container
170 for later use. Pure TiO₂ was also obtained in the same condition without using the
171 biomass precursor.



172
173 **Scheme A:** *Piliostigma* based composite synthesis methods

174 **2.3. Characterisation**

175 The elemental and chemical composition of the materials were determined using X-
176 ray fluorescence spectrometry Fundamental Parameter using ThermoNoran QuanX

177 energy dispersive XRF, while the phases present in addition to indexing the
178 diffraction peaks in the pristine biomass and the produced composites were
179 elucidated by X-ray diffraction through a D8 Bruker spectrometer with $\lambda = 0.15418$ nm
180 at an operating voltage of 40 kV and 30 mA. The diffraction patterns were obtained
181 by scanning between a 2θ range of 10 to 90° using 0.017° each step. The materials
182 were structurally and morphologically characterised on a VEGA3 TESCAN SEM
183 equipment at high resolution. To evaluate the surface chemistry/characteristic groups
184 of the produced materials, Fourier transform infrared (FT-IR) analysis was conducted
185 with an average of 64 scans in the transmission mode from 4000 to 400 cm^{-1} using
186 KBr powder as the diluent for the samples. To investigate the structural changes,
187 Raman spectra were acquired using JobinYvon company Raman spectrometer
188 model T64000. The laser wavelength was 514.5 nm (2.41 eV) and the power set of
189 100 mWatt at room temperature. The surface area was studied using BET method
190 with ASAP 2020 V4.04(V4.04 H) apparatus. Optical absorption of light was evaluated
191 by Cary 300 instrument.

192 **2.4. Batch adsorption experiments**

193 Adsorption experiments were carried out in batch mode. For each run, 20 mL of
194 Cr(VI) solution with the required concentration was added into a 50 mL Erlenmeyer
195 flask and was agitated on a magnetic stirrer (VWR Stirrer) for sufficient time at the
196 constant speed of 400 rpm. Some key operational parameters such as contact time
197 (10 - 80 min), adsorbent dose (0.01 - 0.05 g), initial pH (1.5 - 6) and Cr(VI) concentration
198 (0.4 - 2 ppm) were studied. After the completion of each experiment, the liquid phase
199 was separated from the solid phase by filtration using a microfilter (0.45 μm). The
200 initial and residual Cr(VI) concentrations were quantified using a UV
201 spectrophotometer (SHIMADZU UV-1800, USA 70387) at maximal wavelength value
202 of 540 nm after complexing with a 1.5 -diphenylcarbazide (DPC) solution that was
203 prepared by dissolving 250 mg of DPC in 50 mL ethanol and 200 mL of 1.8 M
204 sulphuric acid. The solution was stirred for 24 h at room temperature and refrigerated
205 at 4 $^\circ\text{C}$ before use. The adsorbed quantity of Cr(VI) per gram of adsorbent, q_e (mg/g)
206 were calculated using Eq. (1):

$$207 \quad q_{e/t} = \frac{(C_0 - C_{e/t})V}{m}$$

208 (1)

209 Where C_o and $C_{e/t}$ are the initial and equilibrium concentration or at specific time of
 210 Cr(VI) solution (mg/L) respectively, V is the total volume of solution (L) and m stands
 211 for the mass of adsorbent (g). The removal yield was also calculated using Eq. (2):

$$\%R = \frac{(C_o - C_e)}{C_o} \times 100$$

(2)

214 Recently, statistical analysis has been considered as one of the most reliable way to
 215 define the best fitting relationship of kinetics study and equilibrium modelling of
 216 adsorption data [38,39]. To identify the best fit model, calculation of chi-squared (χ^2),
 217 adjusted coefficient of determination (adj-R^2) and residual sum of square (RSS) are
 218 recommended [40,41], [38]. Isotherm or kinetic models fit best with experimental data
 219 when the number of parameters increases in which the optimisation of parameters is
 220 accomplished by the minimisation of errors function at a given range. The various
 221 mathematical functions are summarised in Table 2.

Table 2 Statistical functions

Statistical function	Equations	References
Chi-Squared test (χ^2)	$\chi^2 = \sum_{i=1}^n \frac{(q_{e,cal} - q_{e,exp})_i^2}{q_{e,exp}}$	[40]
Residual Sum of Square error (SSE)	$SSE = \sum_{i=1}^n (q_{e,cal} - q_{e,exp})^2$	[39]
Coefficient of détermination (Adj-R ²)	$\text{Adj-R}^2 = 1 - \frac{\sum_{i=1}^n (q_{e,cal} - q_{e,exp})_i^2}{\sum_{i=1}^n [q_{e,cal} - \bar{q}_{e,exp}]_i^2}$	[38]

223

224 **2.5. Photocatalytic activity experiments**

225 The photocatalytic activity of the piliostigma reticulatum decorated TiO₂ based
 226 composites was evaluated by monitoring the degradation of 500 mL of BPB dye
 227 solution in a glass reactor under magnetic stirring. The solution was stirred in the
 228 dark for 30 min to establish adsorption-desorption equilibrium before irradiation. The
 229 residual concentration of the dye solution (V= 3 mL) was measured using a UV
 230 spectrophotometer at regular intervals of time for 3 hours. The effect of some key
 231 operational parameters such as initial dye concentration, oxidising species,
 232 scavengers were performed. The pollutant degradation kinetics was monitored using

233 a SHIMADZU UV-1800 spectrophotometer at the wavelength range between 400 to
234 700 nm.

235 The discoloration potential (%) of BPB dye solution was calculated following Eq. (3):

$$236 \eta(\%) = \frac{(A_o - A_t)}{A_o} \times 100$$

237 (3)

238 Where A_o and A_t are the initial and at time t absorbance intensity peak at maximum
239 wavelength of 592 nm in UV spectrum of BPB respectively.

240 A statistical optimisation for BPB degradation was performed by the Box Behnken
241 Design (BBD) with a desirability function using Expert Design software (UniLaSalle-
242 EME, Rennes, France). According to BBD, 13 sets of experiments instead of 17 were
243 applied to optimise the degradation Yield key parameters, namely catalyst dose
244 (coded as A), pH of solution (coded as B) and interference of NaCl salt (coded as C)
245 with their levels as presented in Table 3.

246 **Table 3** Independent Variables and their levels for experimental design

Variables	levels		
	-1	0	1
A: Catalyst dosage (mg)	200	300	400
B: pH	3	7	11
C: NaCl Concentration (mg/L)	5	10	15

247

248 The BPB dye removal (%) was used as metric to determine the effectiveness of
249 piliostigma decorated TiO_2 based composites as photocatalyst. To eliminate BPB
250 dye, The BPB dye removal (%) was adopted as a response (output) for BBD. In this
251 regard, the degradation experiments were conducted using 6 mg/L of 500 mL BPB
252 dye in a 1000 mL conical flask at a fixed duration of 180 min. After the degradation,
253 the liquid phase was separated from the solid phase by filtration using a microfilter
254 (0.45 μm) and the residual concentration of the dye solution was scanned using a
255 SHIMADZU UV-1800 spectrophotometer. The removal (%) was calculated according
256 to equation (3). Subsequently, an analysis of variance (ANOVA) and a second order

257 quadratic polynomial regression equation was employed to the model response as
258 expressed by Eq. (4):

$$259 \quad S = \alpha_0 + \sum_{i=1}^n \alpha_i m_i + \sum_{i=1}^n \alpha_{ii} m_i^2 + \sum_{1 \leq i < j}^n \alpha_{ij} m_i m_j + \varphi \quad (4)$$

260 Here, S stands for the response of BPB removal (%); α_0 ; α_i ; and α_{ii} are regression
261 coefficient terms for linear and quadratic regression equations. α_{ij} is the interaction
262 coefficient of coded variables m_i and m_j , and φ show the model error.

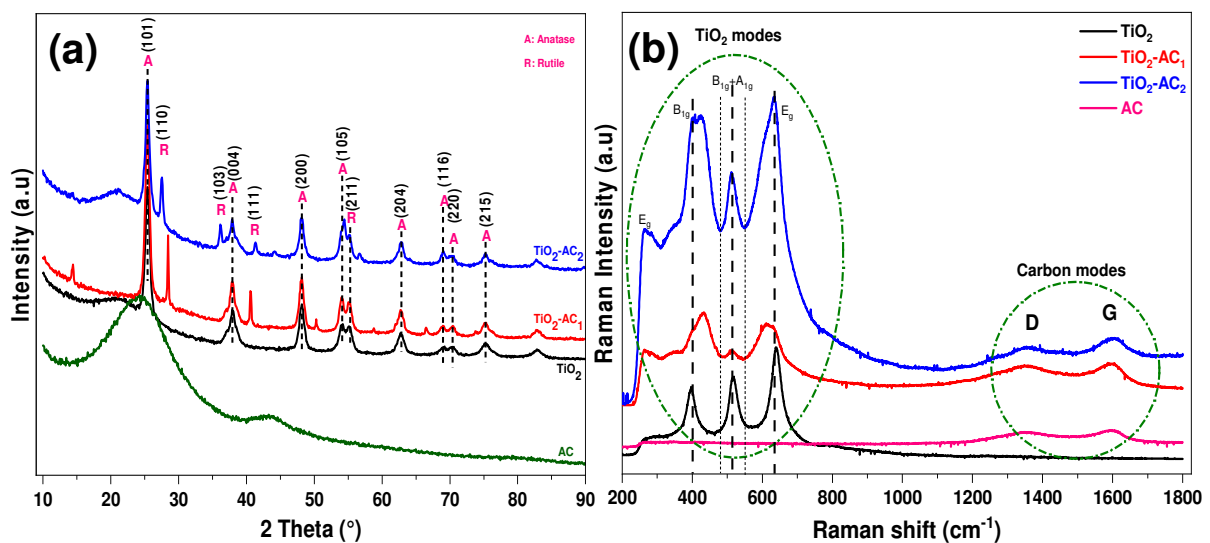
263 3. Results and Discussion

264 3.1. Physicochemical characterisations

265 3.1.1. X-ray Diffraction (XRD) and Raman Spectroscopy analysis

266 XRD analysis was applied to evaluate the phases present and the level of crystallinity
267 of piliostigma reticulatum biomass (PBS), Pure TiO_2 and its derived composites
268 ($\text{TiO}_2\text{-AC}_1$ and $\text{TiO}_2\text{-AC}_2$). The XRD patterns are shown in Fig. (1a). The peaks at 2θ
269 = 15° , 24.45° , 27.70° , 31.13° , 36.48° and 38.32° corresponds to the peaks of
270 crystalline phase present in PBS [42]. The peak of 24.45° was defined as a
271 crystallographic plane of cellulose [43]. Furthermore this results are in agreement
272 with the report of Naik et al [44] when they characterised Canadian biomass for
273 alternative renewable biofuel. The pure TiO_2 and composites ($\text{TiO}_2\text{-AC}_1$ and $\text{TiO}_2\text{-}$
274 AC_2) revealed numerous broad characteristic peaks positioned at $2\theta = 24.45^\circ$, 37.90° ,
275 48.26° , 54.36° , 62.96° , 68.98° , 70.41° , 75.25° corresponding to crystallographic
276 planes of (101), (004), (200), (105), (204), (116), (220), (215) anatase TiO_2 phase
277 (JCPDS 21-1272 and 04-0447) of materials [45–48]. Furthermore, the broad peaks
278 at 27.45° , 36.14° , 41.41° and 55.28° refers to rutile TiO_2 phase (JCPDS 04-0447)
279 present in the materials [49], [50]. significance difference was observed for $\text{TiO}_2\text{-AC}_1$
280 and $\text{TiO}_2\text{-AC}_2$ due to phosphoric chemical activation during $\text{TiO}_2\text{-AC}_2$ synthesis.
281 Moreover, the composites broad numerous reflections peaks. The angle $2\theta = 14.42^\circ$,
282 50.35° , 58.87° , 66.64° ($\text{TiO}_2\text{-AC}_1$) and 36.23° , 44.08° , 56.78° ($\text{TiO}_2\text{-AC}_2$) are ascribed
283 to rutile/anatase TiO_2 , an indication of the formation of rutile and anatase
284 incorporated into graphitic carbon respectively. These results are in agreement with
285 the trend of other reports [51–57]. The crystallinity of the synthesised composites

286 (TiO₂-AC₁ and TiO₂-AC₂) was measured by Raman spectroscopy as shown in Fig.
 287 (1b). It's remarkable that, the spectrum displays the bands at 511 and 634 cm⁻¹
 288 assigned to anatase TiO₂ crystalline phase [58,59], which are related to Raman
 289 active modes: B_{1g}+ A_{1g} and E_g [60], [61] corresponding to O-Ti-O bonding and Ti-O
 290 stretching vibrations [62] respectively. The bands at 263 and 423 cm⁻¹ ascribed to
 291 rutile TiO₂ [63]. In addition to that, we notice the presence of carbon modes at bands
 292 of 1354 cm⁻¹ and 1603 cm⁻¹, which belongs to defects (D) and graphitic (G) structures
 293 of carbon material [57], [64] respectively for the composites. the resulted ID/IG ratio is
 294 0.84 less than 1 indicates a high degree of graphitisation [65] of carbon material in
 295 the composites. This result confirmed the coexistence of carbon and TiO₂ in the
 296 composites materials. The nanoparticles of TiO₂ and composites samples
 297 implemented a Raman peak spectra similar to the characteristic of anatase and rutile
 298 phases of TiO₂ [66], which is in adequate correlation with the XRD patterns presented
 299 earlier. The volumetric fraction of anatase formed in the composites during the
 300 calcination was calculated using the diffraction peak intensities corresponding to 2θ=
 301 25.5° for anatase and 2θ= 27.5° for rutile by applying the method used by pasikhani
 302 et al [67]. According to figure 1, the TiO₂-AC₁ and TiO₂-AC₂ have approximatively
 303 37% of rutile and 63% of anatase phases. The study conducted in this work revealed
 304 that the phosphoric chemical activation of PBS reduces the volumetric fraction of
 305 anatase in the composite. The composite materials with the two crystalline phases
 306 show the band gap energy of 2.8 eV for TiO₂-AC₁ and 2.5 eV for TiO₂-AC₂ compare
 307 to the pure TiO₂ 3.1 eV. This can be beneficial in reducing the recombination of
 308 photo-generated electrons, holes and enhancing photocatalytic ability [67].



309

310

Fig. 1. (a) XRD patterns and (b) Raman Spectra of materials

311

3.1.2. Scanning electron microscopy (SEM) and BET analysis

312

SEM with variable magnifications was performed to study the microstructure of
313 different sections of pristine piliostigma reticulatum (PBS) and the derived composites
314 ($\text{TiO}_2\text{-AC}_1$ and $\text{TiO}_2\text{-AC}_2$). Fig. 2. shows the SEM images of piliostigma biomaterial
315 (PBS) and its composites. According to the morphological features, the obtained
316 micrograph of piliostigma biomass reveals a surface with less pores (Fig. (2a)). The
317 biomass used in this study had almost negligible pores; this observed trend is in
318 agreement with the results obtained by Sahoo et al [43]. Furthermore, it has a
319 uniform shape and size and is highly agglomerated, which may be attributed to the
320 fact that no treatment of the biomass was involved. Fig. 2 (b). shows the SEM image
321 of the PBS based composite, which reveals a high distribution of surface area and
322 the distinct roughness pattern of the TiO_2 clusters deposited (uniformly) on the
323 carbon surface. It is evident from Fig. 2 (c). that the TiO_2 are deposited irregularly
324 and presents more pore size due to phosphoric acid chemical activation used in the
325 synthesis process.

326

The specific surface area was verified by Brunauer-Emmett-Teller theory using the
327 N_2 adsorption-desorption isotherm as summarised in table 4 and figure S1 for
328 hysteresis loops. According to BET results the $\text{TiO}_2\text{-AC}_2$, had a high surface area of
329 $231.961 \text{ m}^2/\text{g}$, while $\text{TiO}_2\text{-AC}_1$ had a lower surface area of $159.681 \text{ m}^2/\text{g}$. This result
330 signified that the $\text{TiO}_2\text{-AC}_2$ composite would be able to better fix contaminants during
331 water treatment process. Furthermore, the phosphoric acid chemical activation of the
332 biomass played an important role to improve the surface area of $\text{TiO}_2\text{-AC}_2$ as can be
333 seen in the SEM spectra (Fig. 2).

334

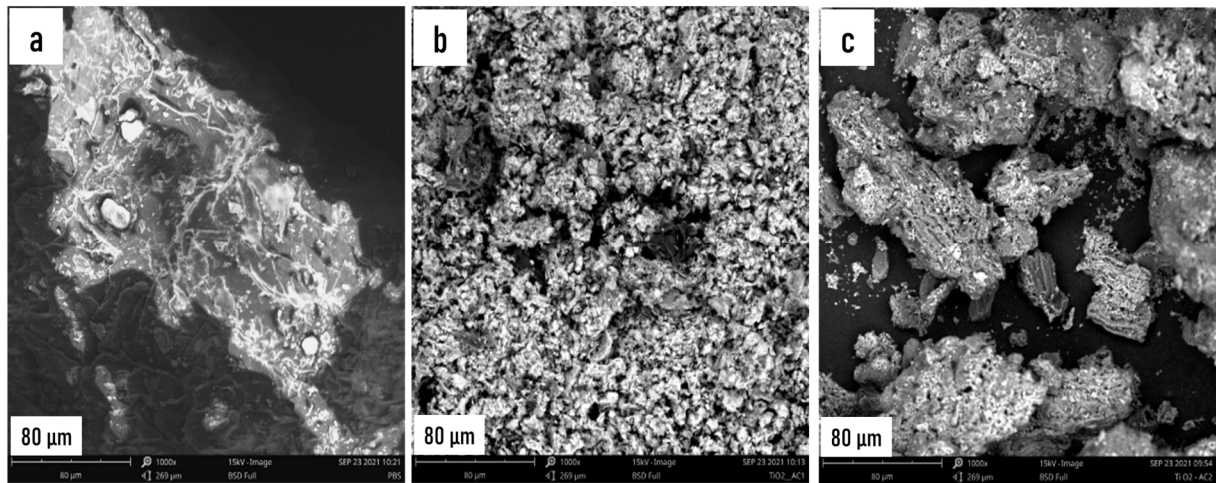


Fig. 2. SEM micrographs of (a) piliostigma biomaterial (PBS), (b) TiO₂-AC₁ and (c) TiO₂-AC₂

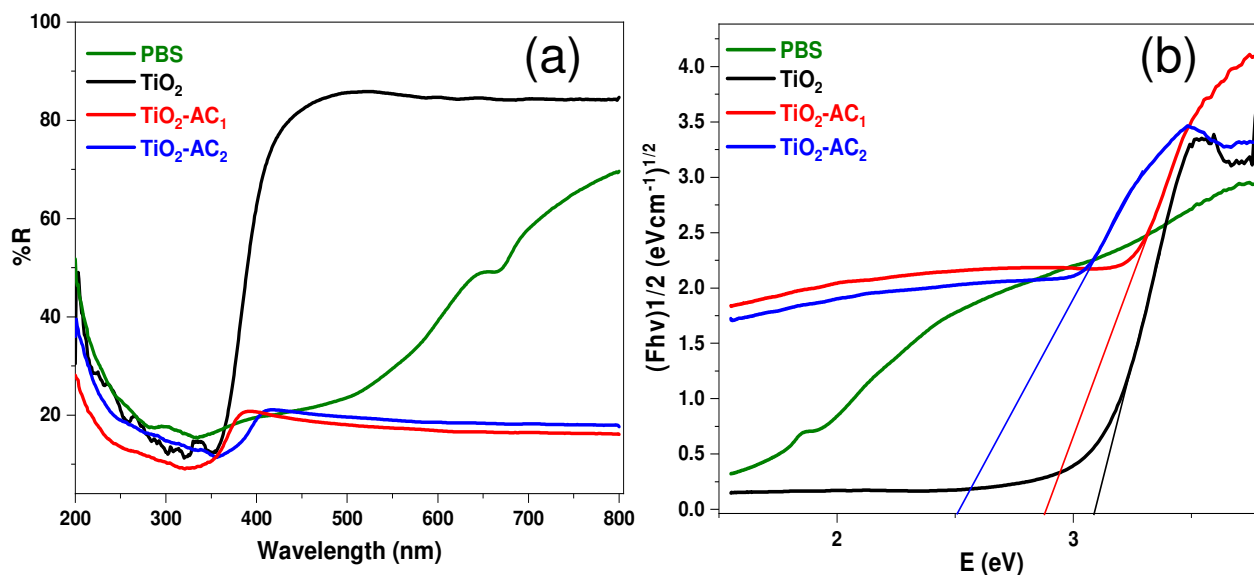
Table 4 Specific Surface Area results

Materials	S _{BET} (m ² /g)	S _{mic} (m ² /g)	S _{Ext} (m ² /g)	Pore Volume (cm ³ /g)	Particle Size (Å)
AC	181.386	129.138	52.248	0.0579	330.785
TiO ₂ -AC ₁	159.681	65.078	94.603	0.0319	375.748
TiO ₂ -AC ₂	231.961	118.374	113.586	0.0536	258.664

S_{BET}: BET surface Area, S_{mic}: Micropore surface Area, S_{Ext}: External surface Area

3.1.3. Optical absorption analysis (UV-vis diffuse reflectance spectroscopy)

Diffuse reflectance spectral analysis (DRS) of the various materials was performed in order to investigate the light absorption and the band gap energy changes of our based composites caused by the addition of activated and non-activated piliostigma biomass. According to the DRS results as implemented in Fig. 3(a). the PBS, TiO₂, TiO₂-AC₁ and TiO₂-AC₂ showed absorption sharp edges at around 650.64, 353.11, 371.32 and 396.01nm respectively. In addition to that, the band gap energy of TiO₂, TiO₂-AC₁ and TiO₂-AC₂ (Fig. 3(b).) were obtained as 3.1, 2.8 and 2.5 eV respectively. It is clear that the TiO₂ and the based composites will absorb in visible region. The gap energy (E_g) decreases for the based composites due to carbon incorporation during thermal treatment and phosphoric chemical activation. Besides, the TiO₂-AC₂ composite revealed high absorption efficiency compare to pure TiO₂ at higher wavelength caused by optimal heterojunction between the basic materials and chemical activation of the biomass before thermal treatment.

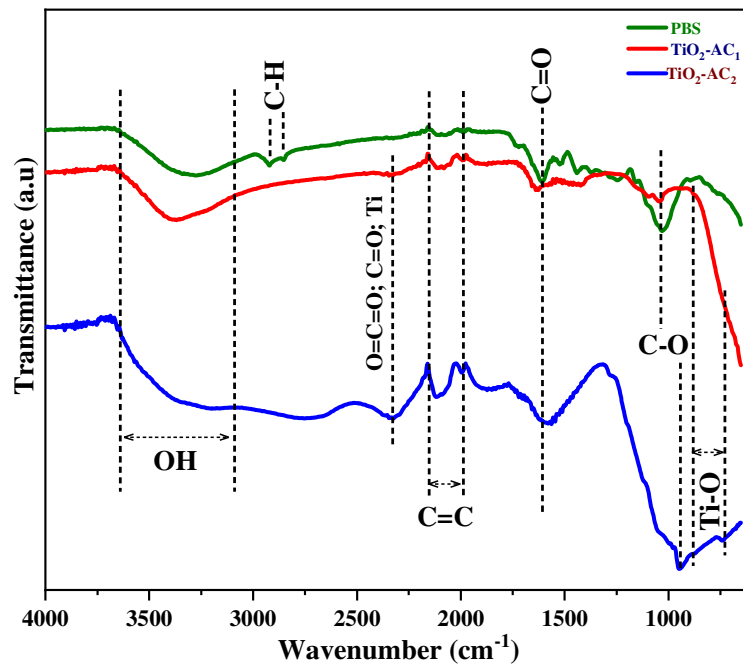


354

355 **Fig. 3.** (a) Diffuse Reflectance Spectra, (b) Plot of transferred Kubelka-Munk versus
 356 energy of PBS, TiO₂ and the derived composites TiO₂-AC₁ and TiO₂-AC₂

357 **3.1.4. Fourier transform infrared spectrophotometry (FTIR)**

358 FTIR spectra of pristine piliostigma and the composites are shown in Fig. 4. The PBS
 359 spectra are typical of lignocellulosic biomass and display a series of very sharp
 360 absorption peaks due to the crystallinity of the samples. As indicated, OH stretching
 361 vibration is depicted at 3277 cm⁻¹ due to the presence of carboxylic acid, alcohol and
 362 moisture [42], [53] while C-H stretching was observed at 2927 cm⁻¹ [7] since no
 363 carbonisation and/or activation of piliostigma was involved. Adsorptions at 1610 cm⁻¹,
 364 1025 cm⁻¹ corresponded to C=O, C-O functional groups signifying the existence of
 365 ketones, ester, carboxylic acids and aldehydes [68]; [42]. The wide band at 2160-
 366 2020 cm⁻¹ is ascribed to C=C of alkenes [69]. The peak at 1448 cm⁻¹ presented the C-
 367 H vibrations indicating alkanes [70] while the peak at 1248 cm⁻¹ were attributed to
 368 C=C of aromatic group. The presence of several functional groups on the surface of
 369 piliostigma biomass as identified by FTIR indicates the potential of this biomaterial to
 370 interact with pollutants (Cr (VI) and BPB in solution). Furthermore, the composites
 371 spectrum shows specific peaks around 738 to 935 cm⁻¹ corresponding to Ti-O
 372 absorption group [71,72], [53] that is due to TiO₂ loaded on the carbon. The peak at
 373 2335 cm⁻¹ is related to the asymmetric stretching vibration of the O=C=O group [73]
 374 which can play the role of an electron donor is formed during the synthesis process.
 375 Others reports from literature ascribed to the peak at 2335 cm⁻¹ the C=O [74] and Ti
 376 [73].



377

378 **Fig. 4.** FTIR spectra of piliostigma biomaterial (PBS) and composites

379 **3.1.5. X-ray fluorescence spectrometry fundamental parameters (XRS-FP)**

380 To better understand the chemical and elemental composition of piliostigma and the
 381 derived composites, XRS-FP was performed to identify inorganic elements and
 382 mineral matters. In the present study, for most part, piliostigma biomass implied high
 383 concentrations of O, Ca, K, Mg, Al, Cl and minor concentrations of Si, S, Fe as
 384 tabulated in Table 5. Similar results were reported by Sahoo et al [75] who
 385 characterised non-edible lignocellulosic biomass to elucidate their biofuel production
 386 potential. These metalloid elements were also detected by Oo et al [76] in the forest
 387 and sugarcane leaf biomass. On the contrary, the piliostigma based composites
 388 (TiO₂-AC₁ and TiO₂-AC₂) showed maximum contents of O, Ti, Cl for TiO₂-AC₁ and P
 389 for TiO₂-AC₂ with a lower percentage of other elements. This result confirmed the
 390 presence of TiO₂ in the composite, as shown earlier by SEM micrographs on the
 391 derived composites.

392

Table 5 Elemental composition of piliostigma biomaterial

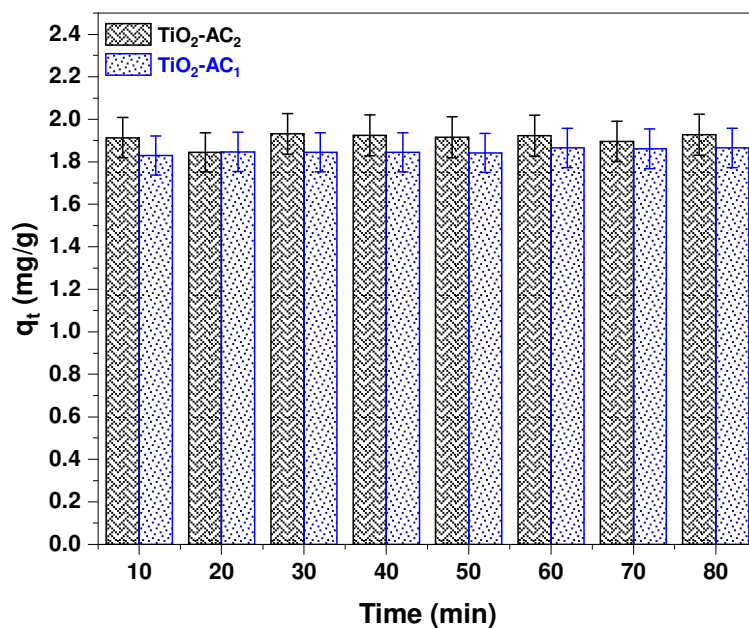
Materials	Elements	O	Mg	Al	Fe	S	Cl	K	P	Ti	Si	Ca	Others
PBS		32.30	15.19	4.81	1.18	1.63	3.33	17.83	00.62	00.12	2.05	19.84	1.10
TiO ₂ -AC ₁	wt (%)	34.87	03.39	2.35	0.37	0.26	8.21	05.88	00.45	37.05	0.86	05.01	1.30
TiO ₂ -AC ₂		45.39	00.25	1.97	0.62	0.04	1.15	10.50	23.64	12.80	0.58	02.14	0.94

393

394 3.2. Adsorption tests results

395 3.2.1. Effect of contact time

396 Equilibrium time is one of the most important parameters in evaluating the efficiency
397 of an adsorbent. It informs about the removal rates of the pollutants in adsorption
398 process. It is known that high removal at short contact time reveals that film diffusion
399 is a controlling reaction step while high removal at long contact time indicates that
400 intraparticle diffusion may be the controlling step [77]. The adsorption of Cr(VI) onto
401 piliostigma decorated TiO₂ based composites at initial concentration of 2 mg/L was
402 studied as a function of contact time to reach the adsorption equilibrium time (Fig. 5.).
403 The results reveal that about 98% and 99% of Cr(VI) was adsorbed with the
404 maximum uptake capacity of 1.86 and 1.93 mg/g at an equilibrium time of 30 min by
405 TiO₂-AC₂ and TiO₂-AC₁ composites respectively as observed by [78]. These results
406 indicate that film diffusion and chemical adsorption contribute to the rate determining
407 step. Liu et al observed a similar trend when removing Cr(VI) ions in aqueous
408 solution with zeolite/chitosan composites [79].

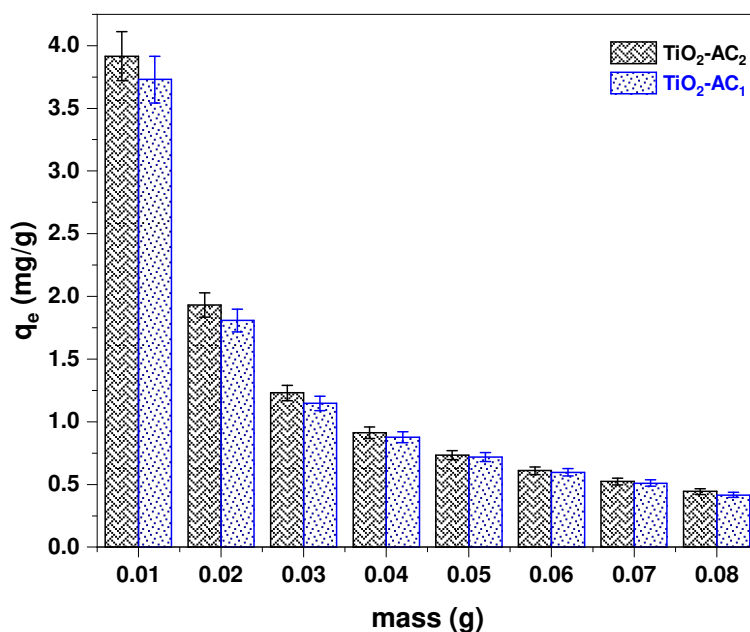


409
410 **Fig. 5.** Effect of contact time for Cr(VI) adsorption. Conditions : m=0.02 g; pH=1.5;
411 Conc=2 mg/L; T=20°C.

412 3.2.2. Effect of adsorbent dose

413 Catalyst dose is considered as a key factor for choosing a catalytic material for the
414 removal of inorganic wastes. A high uptake of pollutants on limited material

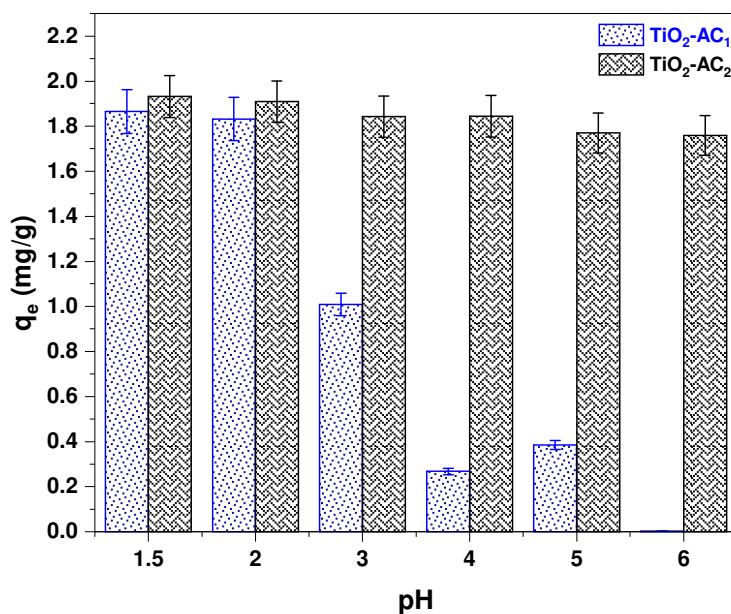
415 (adsorbent) quantities and the establishment of equilibrium means high efficiency of
 416 the adsorbent towards the removal of inorganic contaminants. This can shows the
 417 ability of our composites for a quantitative removal of Cr(VI) of initial concentration of
 418 2 mg/L. The observed trend of a small decrease in removal percentage and the
 419 decrease in adsorption capacity with the increase of both composites dose is shown
 420 in Figure 6. Decreasing the removal percentage of Cr(VI) by raising the mass of
 421 catalyst is observed, reaching a percentage of 89% and 91% with 0.04 g of $\text{TiO}_2\text{-AC}_2$
 422 and $\text{TiO}_2\text{-AC}_1$ can be observed in Fig. 6. respectively. However, a decrease of the
 423 adsorbed amount is shown with the addition of adsorbent dose. The optimum uptake
 424 capacity is obtained with a catalyst dose of 0.01 g for a volume 20mL. These results
 425 imply that a small decrease of the adsorption percentage with a raising adsorbent
 426 dose is due to the formation of aggregates that reduce access to some active sites
 427 for a given concentration. The higher uptake quantity of pollutants at lower adsorbent
 428 mass is attributed to the optimal dispersion of adsorbent in the medium with absence
 429 of the formation of aggregate that would mask some active sites [78]. This trend is
 430 in agreement with the report of Almeida et al [80], who mad same assumption on
 431 chemically activated red mud for hexavalent chromium adsorption.



432
 433 **Fig. 6.** Effect of adsorbent dosage for Cr(VI) adsorption. Conditions : $t=30$ min ;
 434 $\text{pH}=1.5$; $\text{Conc}=2$ mg/L ; $T=20^\circ\text{C}$.

435 **3.2.3. Effect of pH**

436 The solution pH is the second most important key operational parameter that
437 influences the electrostatic interactions of adsorbents and pollutants in solution
438 during the adsorption process. Electrostatic interactions are closely related to the pH
439 value because it determines the form of Cr(VI) chemical specifications and modifies
440 some functional groups by ionisation. The pH value affects, the surface charge on the
441 adsorbent. As illustrated in Fig. 7., the adsorption capacity and the removal
442 percentage of Cr(VI) on the piliostigma based composites decrease from 1.93 to
443 0.002 mg/g (TiO₂-AC₁); 1.86 to 1.75 mg/g (TiO₂-AC₂) and 96.57 to 0.11 % ; 93.25 to
444 87.94% with increase of pH from 1.5 to 6. This trend shows that the lower pH of
445 solution favours the Cr(VI) adsorption on TiO₂-AC₁ and TiO₂-AC₂ respectively due to
446 the ionic nature of Cr(VI) molecules. Similar results of steady decrease of Cr(VI)
447 adsorption with raising pH was also cited in literature [14]. TiO₂-AC₁ composite has
448 lower adsorption capacity of Cr(VI) at high pH which can be attributed to a decrease
449 in the extent of ionic bond formation and weaker ion-dipole interactions [81] while
450 TiO₂-AC₂ composite show a less decrease in adsorption capacity. More so, there is
451 competition between hydroxyl ions and Cr(VI) ions for the occupations of adsorption
452 sites near neutral and alkaline conditions. Masinga and co-authors draw similar
453 conclusions during the removal of Cr(VI) ions by polyethyleneimine impregnated
454 activated carbon [82]. This result confirms the fact that Cr(VI) ion adsorption is
455 favourable at acidic pH for TiO₂-AC₁ [83], but TiO₂-AC₂ offers the possibility to work
456 near neutral pH value which are close to pH values of real industrial wastewater and
457 surface water due to phosphoric chemical activation used in the route 2.

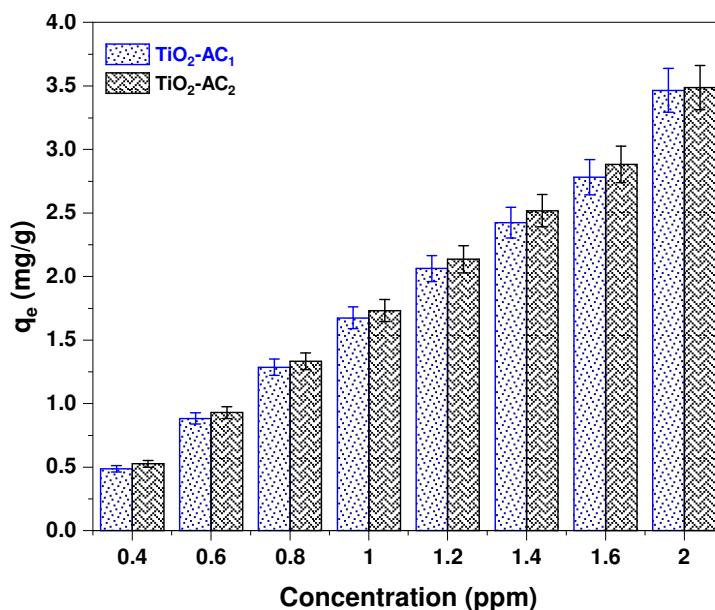


458

459 **Fig. 7.** Effect of pH for Cr(VI) adsorption. Conditions : t=30 min; m=0.02 g; Conc=2
 460 mg/L; T=20°C.

461 **3.2.4. Effect of Cr(VI) initial concentration**

462 A given mass of piliostigma based composites can adsorb only a certain amount of
 463 Cr(VI) ions, that's why the initial dye concentration plays an important role and
 464 provides an essential driving force for mass transfer between the adsorbate and solid
 465 phases in the adsorption process. The effect of initial concentration on adsorption of
 466 Cr(VI) ions was studied. As evident from the results depicted in Fig. 8., the uptake
 467 capacity increased with the increase in the initial concentration, whereas the removal
 468 percentage shows a saturation plateau at a concentration of 1.6 mg/L for a given
 469 catalyst dose of 0.01 g that emerged from the total occupation and saturation of
 470 surface-active sites upon increasing Cr(VI) ions concentration. The higher absorbed
 471 quantity is ascribed to greater interaction of Cr(VI) ions with active groups on the
 472 surface of the composites, resulting from the higher availability of pollutants that
 473 occupied the maximum sites. However, we noticed that the simultaneous saturation
 474 plateau of the removal percentage could be due to the fact that, the considered mass
 475 become saturated at higher concentrations, leaving less residual Cr(VI) ions behind
 476 in solution. The results agree with the observations in literature [82], [84,85].



477

478 **Fig. 8.** Effect of initial Cr(VI) ions concentration. Conditions : $t=30$ min ; $m=0.01$ g ;
479 $pH=1.5$; $T=20^{\circ}C$.

480 **3.3. Kinetics modelling analysis**

481 Kinetics study is a vital aspect that helps for understanding the reaction mechanism
482 of Cr(VI) adsorption on piliostigma based composites. It is an important tool to
483 optimise the design of an adsorption system in terms of economics and efficiency.
484 Best fitting of experimental data was evaluated by four reaction control models:
485 pseudo-first order, pseudo-second order, Elovich and intraparticle diffusion. All
486 equations are summarised in Table 6 below.

487

Table 6 Nonlinear kinetics model equations

Kinetic models	Non-linear form	References
Pseudo first order	$q_t = q_e [1 - \exp(-K_1 t)]$	[14]
Pseudo second order	$q_t = \frac{q_e^2 K_2 t}{1 + q_e K_2 t}$	[5]
Elovich	$q_t = \frac{1}{\beta} \ln(1 + \alpha \beta t)$	[24]
Intraparticle diffusion	$q_t = k_{int} \sqrt{t} + c$	[86]

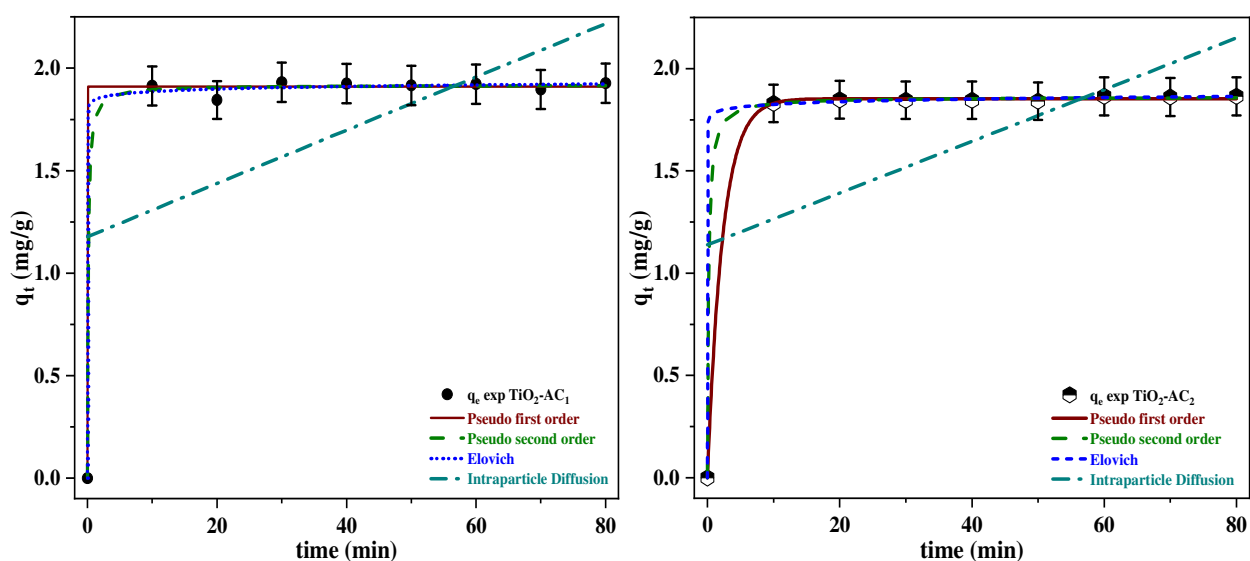
488

489 where q_t and q_e ($mg.g^{-1}$) are the adsorbed capacities at a time t and at equilibrium
490 respectively. k_1 (min^{-1}) is the rate constant of pseudo first order and k_2 ($g.mg^{-1}min^{-1}$)
491 is the rate constant of pseudo-second order of the adsorption process. k_{int} is the
492 intraparticle diffusion rate constant ($mg.g^{-1}.min^{-1/2}$) and c represents the value of the

493 thickness of the boundary layer ($\text{mg}\cdot\text{g}^{-1}$). α refers to the initial adsorption rate ($\text{mg}\cdot\text{g}^{-1}$
494 $\cdot\text{min}^{-1}$) and β is related to the activation energy for chemisorption ($\text{g}\cdot\text{mg}^{-1}$).

495 The kinetic parameters derived from fitting the adsorption data of Cr(VI) are shown in
496 Table 7 and the representative nonlinear plots are presented in Fig. 9. As can be
497 observed, the adsorption of Cr(VI) on piliostigma based composites showed good
498 nonlinear fit of pseudo-first order, pseudo-second order and Elovich rather than
499 intraparticle diffusion. It seems from the linear fitting of intraparticle diffusion model
500 (figure S2) that film diffusion is a controlling reaction step in Cr(VI) adsorption
501 process [77].

502 The R^2 (0.99) value is closer to 1 and the calculated uptake capacity (q_{ecal}) of
503 pseudo-second order matched well with the experimental data (q_{exp}) and present
504 lower errors analysis values (Table 8) [80]. These results lead to the conclusion that
505 there is a high affinity and fast bonding of Cr(VI) ions molecules to the surface of
506 piliostigma based composites. In addition, the rate constant K_2 is higher than the
507 others (K_1 , K_d) indicating faster equilibrium of Cr(VI) ions uptake as desired in
508 adsorption systems for practical applications in industrial wastewater treatment. The
509 lowest value of thickness shows that the intraparticle diffusion does not contribute to
510 the rate determining step as determined by low contact time. This study suggests
511 that, the adsorption process follows a chemisorption mechanism as can be confirmed
512 by FTIR results on the surface functional groups, XRS-FP results on the various
513 components that can provide electrostatic interactions and SEM imaging which
514 confirms the presence of surface area and pores.



515

516

Fig. 9. Nonlinear plot of kinetic models

517

Table 7 Calculated parameters for kinetics of Cr(VI) adsorption

Materials	q_{exp}	Pseudo first order			Pseudo second order			Intraparticle diffusion			Elovich		
		R^2	q_m	k_1	R^2	q_m	k_2	R^2	k_d	C	R^2	B	α
TiO ₂ -AC ₁	1.93	0.99	1.90	8.84E+10	0.99	1.92	4.42	0.31	0.026	1.17	0.99	55.63	6.58E+42
TiO ₂ -AC ₂	1.86	0.99	1.85	0.44	0.99	1.86	2.95	0.31	0.025	1.14	0.99	53.40	3.99E+39

518

519

Table 8 Statistical results of kinetics study

Kinetics model/Materials	χ^2	RSS	Total	adj-R ²
TiO₂-AC₁				
pseudo first order	0.00080	0.00600	0.0068	0.99
pseudo second order	0.00075	0.00500	0.0058	0.99
Intraparticle diffusion	0.32000	2.23000	2.55	0.21
Elovich	0.00073	0.00500	0.0057	0.99
TiO₂-AC₂				
pseudo first order	0.00009	0.00065	0.0007	0.99
pseudo second order	0.00007	0.00046	0.0005	0.99
Intraparticle diffusion	0.29000	2.08000	2.37	0.21
Elovich	0.00006	0.00040	0.0004	0.99

520

521 **3.4. Analysis of the equilibrium modelling of isotherms**

522 Adsorption isotherm modelling represents the mathematical relation of uptake
 523 capacity of the target molecule per gram of catalyst as a function of the equilibrium
 524 concentration at equilibrium and at a certain temperature. It reveals information about
 525 the surface properties of the adsorbent and removal mechanism of the target
 526 molecule, in our case the Cr(VI) ions. The equilibrium data of Cr(VI) ions are
 527 analysed by 2, 3, and 4 parameters isotherm models. The regression equations of
 528 both models are shown in Table 9.

529

Table 9 Nonlinear isotherm models equations

Isotherm model	Non-linear form	References
Two parameter models		

Langmuir	$q_e = \frac{q_m K_L C_e}{1 + K_L C_e}$	[87,88]
	$R_L = \frac{1}{1 + K_L C_0}$	
Freundlich	$q_e = k_f c_e^{1/n}$	[89]
Temkin	$q_e = b_T \ln(K_T C_e)$	[90]
Three parameter models		
Sips	$q_e = \frac{K_s C_e^{ns}}{1 + a_s C_e^{ns}}$	[91]
Redlich-Peterson	$q_e = \frac{ArC_e}{1 + KRC_e^n}$	[92]
Toth	$q_e = \frac{K_T C_e q_m}{[1 + (K_T C_e)^n]^{\frac{1}{n}}}$	[91]
Khan	$q_e = \frac{q_m b_k C_e}{(1 + b_k C_e) a_k}$	[91]
BET	$q_e = \frac{q_m K_s C_e}{(1 + K_s C_e)(1 - K_L C_e + K_s C_e)}$	[93]
Four parameter models		
Baudu	$q_e = \frac{q_m b_0 C_e^{1+x+y}}{1 + b_0 C_e^{1+x}}$	[92,93]
Fritz-schlunder	$q_e = \frac{q_{mFS} K_{FS} C_e}{1 + q_{mFS} C_e^{M_{FS}}}$	[94], [38]
Marczewski-jaroniec	$q_e = q_{MJ} \left[\frac{(K_{MJ} C_e)^{n_{MJ}}}{1 + (K_{MJ} C_e)^{n_{MJ}}} \right]^{m_{MJ}/n_{MJ}}$	[41], [38]

530

531 The Langmuir model assumes a monolayer adsorption mechanism where the
532 adsorbent disposes of a fixed number of active sites of similar activation energy and
533 affinity towards the adsorbate. In this model, the steric limitation between the
534 adjacent adsorbate species is ignored [87]. q_{max} and K_L are the Langmuir constants
535 which are related to the adsorption capacity. The Freundlich adsorption isotherm
536 suggests a multilayer adsorption mechanism where various sites with different
537 adsorption energies are involved [89]. It is assumed that the heterogeneous surface
538 of the adsorbent exhibits non-uniform distribution of adsorption heat instead of
539 exponential decrease upon the end of the adsorption process. K_F and n are the

540 Freundlich constants which are related to the adsorption capacity and intensity. The
541 Temkin isotherm contains a factor that explicitly considers adsorbent-adsorbate
542 interactions. The model assumes that the heat of adsorption of all molecules in the
543 layer reduces in a linear way rather than in a logarithmic coverage [90]. Furthermore,
544 b_T is the constant of adsorption energy, T is the temperature (K), K_T is binding
545 constant at equilibrium ($L.g^{-1}$).

546 The Sips and Redlich-Peterson models are hybrid models combining Langmuir and
547 Freundlich models. They have been frequently applied to describe adsorption in
548 homogeneous and heterogeneous systems [91]. K_R , a_R and n are Redlich-Peterson
549 parameters while q_m , K_S and n_s are Sips parameters. The Toth model is developed to
550 widen the application of the Langmuir model in heterogeneous systems. It assumes
551 that the adsorption energy of most adsorption sites is smaller than the mean energy
552 [92]. q_m is the adsorption capacity, K_T is the Toth constant and n is a component that
553 describes the degree of heterogeneity of the adsorption systems. The Khan model is
554 a generalised isotherm dedicated to the adsorbate adsorption from pure solutions, in
555 which both Langmuir and Freundlich models are represented. It was established for
556 single-and multi-component adsorption systems [91]. The BET isotherm model is a
557 special form of Langmuir isotherm extended to derive multilayer adsorption systems
558 in liquid-solid interface. It uses the same assumptions applied in Langmuir model with
559 the addition of second, third and higher layers having the same energy of adsorption
560 which equals heat of fusion, and are not influenced directly by adsorbent-adsorbate
561 interactions [93].

562 The Fritz-Schlunder isotherm is an empirical equation of Langmuir-Freundlich type to
563 which a wide range of experimental results can fit due to a large number of
564 coefficients in the model [38], [93,94]. Nonlinear regression analysis can be used to
565 determine the isotherm parameters [92]. The Bauder isotherm is the reduced form of
566 the Langmuir model taking into account that the Langmuir coefficients are not
567 constant in a broad range. For lower surface coverage, the Bauder isotherm model is
568 the reduced form of the Freundlich model [38], [92,93]. The Marczewski-Jaroniec
569 isotherm resembles to the Langmuir model. It is the recommended model of local
570 Langmuir isotherm and adsorption energies distribution in the active sites of
571 adsorbent [41], [92,93], [38].

572 The related non-linear plots that correspond to these isotherms are presented in Figs.
573 10.,11.,12. and the calculated parameters are collected in Tables 10,11,12. As shown
574 in Fig. 10., none of the two-parameter isotherms fitted optimally the experimental
575 data for either of the composites as reflected by the lowest R^2 (Table 10). On the
576 other hand, the Sips model (Table 11) shows a good correlation with the experimental
577 data as reflected by the high R^2 (0.92 and 0.93) for $\text{TiO}_2\text{-AC}_1$ and $\text{TiO}_2\text{-AC}_2$
578 respectively. The calculated values of adsorption capacity ($q_{e,\text{cal}}= 3.25$ and 3.53) are
579 closer to the experimental values ($q_{e,\text{exp}}= 3.46$ and 3.49). The n_s constant of the Sips
580 model reflects the high affinity of the Cr(VI) ions molecules with the piliostigma based
581 composites, most probably due to high electrostatic interaction. The highest value of
582 K_s indicates multilayer binding of Cr(VI) ions molecules onto heterogeneous surface
583 of piliostigma based composites attributed to organic and inorganic components
584 present on the surface of the adsorbent, a hypothesis confirmed by the results of
585 FTIR and XRS-FP. Besides, the Marczewski-Jaroniec four parameter isotherm
586 (Table 12) shows a higher R^2 (0.93) than that of the Sips model for $\text{TiO}_2\text{-AC}_1$ with
587 good prediction of experimental data. According to the errors analysis (Table 13) the
588 isotherm that fitted best the experimental data is the Marczewski-Jaroniec for $\text{TiO}_2\text{-}$
589 AC_1 and Sips for $\text{TiO}_2\text{-AC}_2$, based on the lower value of the errors function and good
590 adjusted- R^2 which shows satisfactory correlation between predicted and
591 experimental results. The adsorption capacity of piliostigma based composites were
592 compared with other adsorbents previously applied for the adsorption of Cr(VI) ions
593 molecules, presented in Table 14. Although the prepared composites in this work
594 achieved lower adsorption capacity compared to numerous adsorbents in the
595 literature, its adsorption capacity is much higher than ARM-HCl, ARM-HNO₃ (2.44
596 and 2.65 mg/g) for concentrations higher than the one of the present work [80].
597 Furthermore, the prepared $\text{TiO}_2\text{-AC}_2$ composite offers the possibility to proceed at pH
598 6 which is suitable for industrial real wastewater. The simple, abundant and eco-
599 friendly nature of the prepared composites is their main advantage for practical
600 applications.

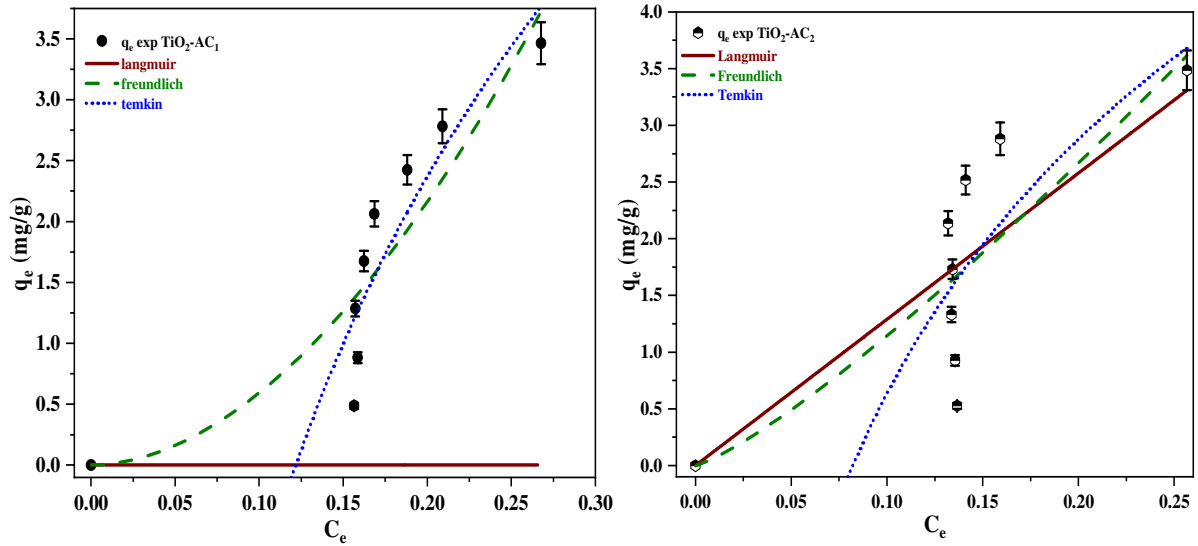


Fig. 10. Nonlinear plot of 2 parameter isotherm models.

Table 10 Calculated parameters isotherm of Cr(VI) adsorption

2 parameter Isotherms	Materials	Calculated parameters				
Langmuir	TiO ₂ -AC ₁	0	-3.73	0	R ²	R _L
	TiO ₂ -AC ₂	11225	0.001	0.64		
Freundlich	TiO ₂ -AC ₁	43.66	1.86	0.73	R ²	
	TiO ₂ -AC ₂	19.02	1.22	0.49		
Temkin	TiO ₂ -AC ₁	4.78	8.22	0.87	R ²	
	TiO ₂ -AC ₂	3.23	12.18	0.67		

601

602

603

604

605

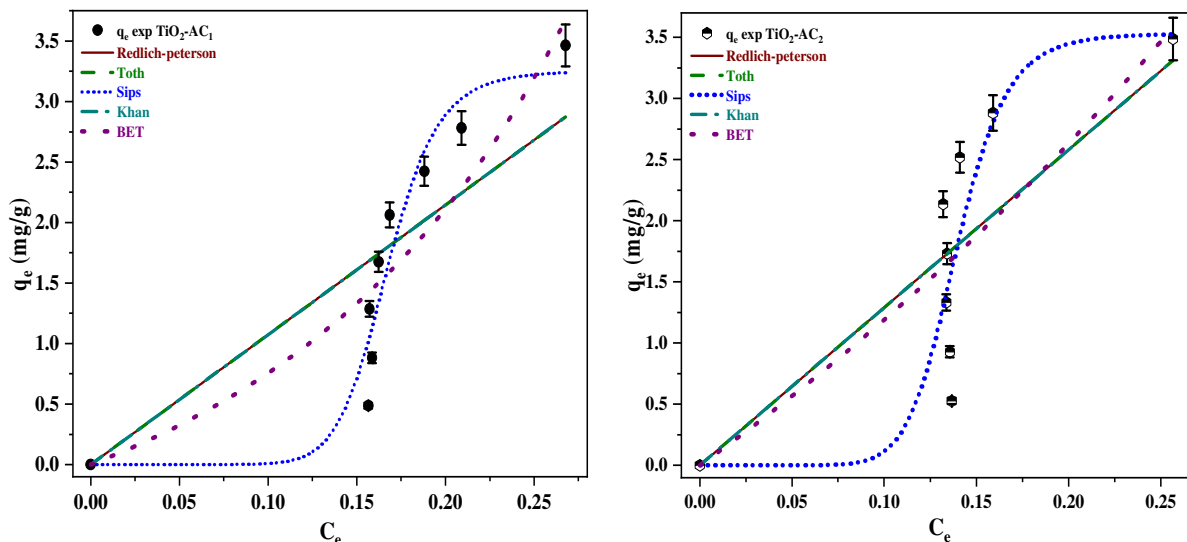
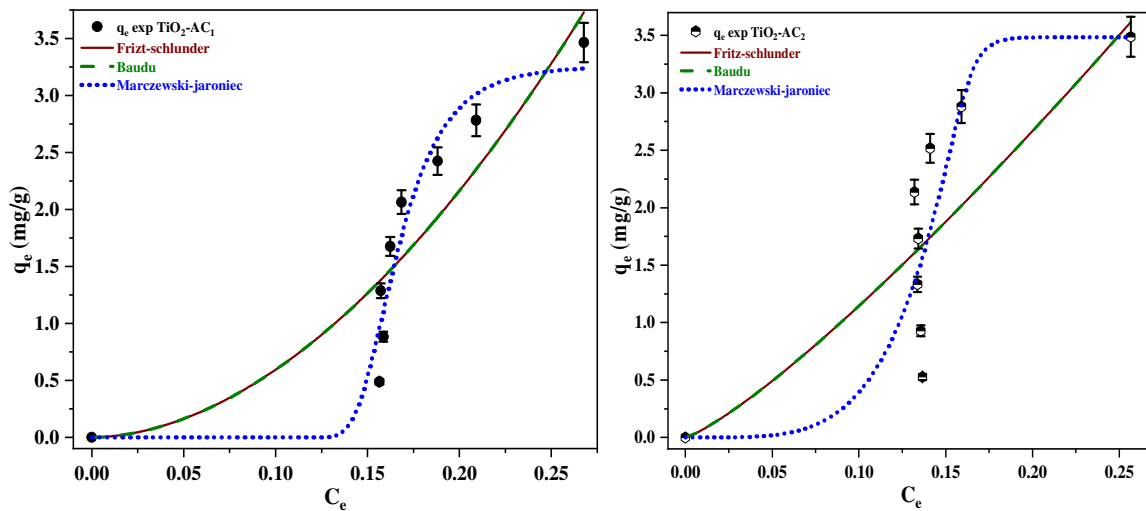


Fig. 11. Nonlinear plot of 3 parameter isotherm models.

Table 11 Calculated parameters isotherm of Cr(VI) adsorption

3 parameter						
Isotherms	Materials	Calculated parameters				
Sips	TiO ₂ -AC ₁	3.25	5.97	11.61	R ²	0.92
	TiO ₂ -AC ₂	3.53	7.18	10.26		
Redlich-Peterson	TiO ₂ -AC ₁	10.73	0.0001	4.62E+09	R ²	0.69
	TiO ₂ -AC ₂	12.9	0.01	24.05		
Toth	TiO ₂ -AC ₁	4.78E-04	0.49	1.09E-05	R ²	0.69
	TiO ₂ -AC ₂	0.025	0.027	2.67E-05		
Khan	TiO ₂ -AC ₁	3.38	3.16	7.09E-15	R ²	0.69
	TiO ₂ -AC ₂	3.4	3.78	1.77E-14		
BET	TiO ₂ -AC ₁	305.78	1.80E-02	1.34	R ²	0.79
	TiO ₂ -AC ₂	56.9	0.19	5.60E-01		

610



611

612

Fig. 12. Nonlinear plot of 4 parameter isotherm models.

613

614

Table 12 Calculated parameters isotherm of Cr(VI) adsorption

4 parameter Isotherms	Materials	Calculated parameters						
		q_m	K	y	x	R^2		
Baudu	TiO ₂ -AC ₁	7.005	6.23	0.51	0.35	0.81		
	TiO ₂ -AC ₂	4.19	4.53	-86.83	87.05		0.65	
Fritzsche-schlunder	TiO ₂ -AC ₁	0.000	43.63	4.46E+09	1.86	0.82		
	TiO ₂ -AC ₂	19.01	0.01	23.06	1.22		0.65	
Marczewski-jaroniec	TiO ₂ -AC ₁	31.18	8.55	9.56	20.4	0.93		
	TiO ₂ -AC ₂	95.71	6.11	27.47	0.16		0.75	

615

616

Table 13 Statistical results of equilibrium modelling

Isotherm models/Materials	χ^2	RSS	Total	adj-R ²	Isotherm models/Materials	χ^2	RSS	Total	adj-R ²
TiO₂-AC₁					TiO₂-AC₂				
Two parameter model					Two parameter model				
Langmuir	3.89	6.98	10.87	-0.16	Langmuir	0.53	3.75	4.28	0.58
Freundlich	0.31	1.84	2.15	0.69	Freundlich	0.6	3.6	4.2	0.4
Temkin	0.17	1.25	1.42	0.85	Temkin	0.47	3.35	3.82	0.63
Three parameter model					Three parameter model				

Redlich-peterson	0.52	3.13	3.65	0.58	Redlich-peterson	0.52	3.75	4.27	0.62
Toth	0.52	3.13	3.65	0.58	Toth	0.52	3.75	4.27	0.62
Sips	0.13	0.79	0.92	0.61	Sips	0.45	2.71	3.16	0.9
Khan	0.52	3.13	3.65	0.58	Khan	0.62	3.75	4.37	0.52
BET	0.33	2.03	2.36	0.73	BET	0.61	3.63	4.24	0.54
Four parameter model					Four parameter model				
Frizt-Schlunder	0.36	1.84	2.2	0.71	Frizt-Schlunder	0.72	3.6	4.32	0.44
Baudu	0.36	1.84	2.2	0.71	Baudu	0.72	3.6	4.32	0.44
Marczewski-Jaroniec	0.13	0.68	0.81	0.91	Marczewski-Jaroniec	0.53	2.65	3.18	0.59

617

618 **Table 14** Comparative table of operational parameters and adsorption capacities for
619 the removal of Cr(VI) by other alternative adsorbents.

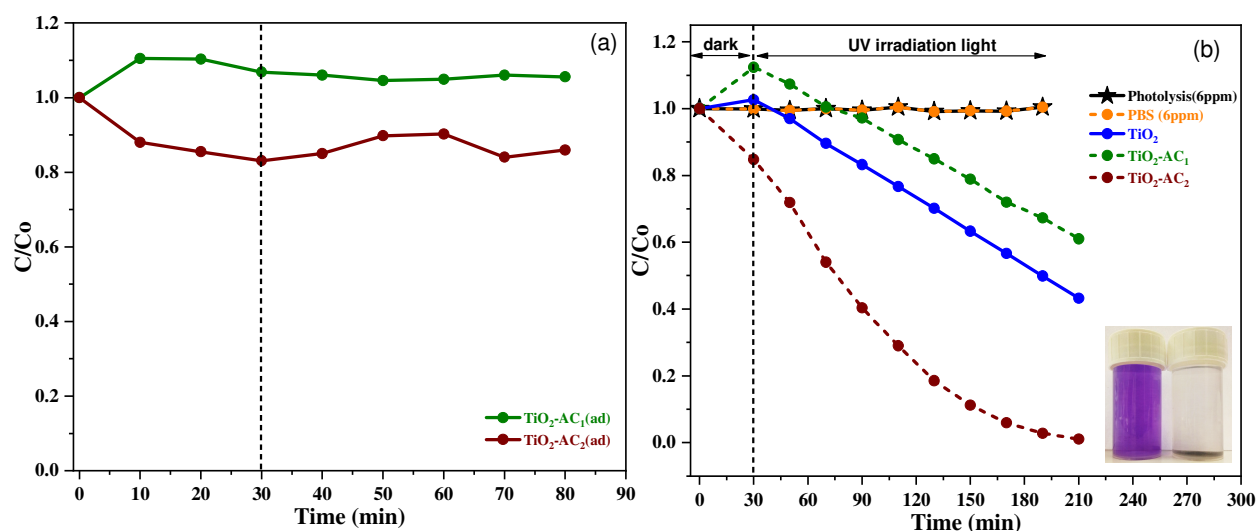
Catalyst	pH	Dosage (g)	Concentration (mg/L)	Time (min)	q_e (mg/g)	References
ARM-HCl	4.4	0.22	10	30	2.94	[80]
ARM-HNO ₃	5.2	0.23	12	30	2.65	[80]
ACAP	2	0.5	50	120	36.01	[81]
Corn Straw	6.5	0.5	200	120	116.97	[85]
MAC-PEI	2	1	200	120	114	[82]
Groundnut shells	2	2	13	80	131	[95]
Corn stalks derived-ACs	4.5	2.5	300	150	89.5	[28]
Maghemite Nanoparticles	2.5	0.1	5	22	4.15	[96]
AC/nZVI	4	1.5	15	1440	6.67	[97]
NCNB	4	1	1000	90	2749.68	[98]
Fe/ZnFe ₂ O ₄ -MNB	1	0.05	7	150	13.92	[99]
GEO	2	0.05	50	60	27.78	[100]
OCNOs	2	0.025	100	720	26.53	[101]
TiO ₂ -AC ₁	1.5	0.01	2	30	3.46	Present study
TiO ₂ -AC ₂	1.5	0.01	2	30	3.49	Present study

620

621 **3.5. Photocatalytic ability of *piliostigma reticulatum* based composite**

622 The photocatalytic efficiency of the synthesised catalysts under UV irradiation was
623 assessed by choosing BPB as pollutant model. To reasonably evaluate the
624 photocatalytic activity of the composites, blank experiments and adsorption tests (Fig.
625 13.(a)), were conducted to evaluate BPB degradation under UV light, biomass
626 activity, TiO₂ and composites adsorption of BPB. As shown in Fig. 13.(b), the light
627 and biomass (PBS) have negligible effect on the degradation of BPB. Thereby,
628 degradation of BPB by photolysis and pristine PBS can be ignored as shown by
629 [102]. For the adsorption study, the pure TiO₂ and TiO₂-AC₁ composite exhibited
630 considerable secondary reaction with BPB while the TiO₂-AC₂ composite presented
631 low adsorption efficiency as compared to its catalytic capability, hence surface
632 adsorption did not play an important role in the elimination of BPB dye. Therefore, the
633 degradation activity of TiO₂-AC₂ composite can be evaluated. The TiO₂-AC₁
634 composite was not used for further study due to the fact that the raising of
635 absorbance in BPB spectra may be due to TiO₂-AC₁ reaction/complexation with BPB
636 chromophore and the appearance of an intermediate adsorbing light at the same
637 wavelength. In comparison with pure TiO₂ obtained from the same procedure of
638 synthesis, TiO₂-AC₂ composite shows better photocatalytic efficiency with 100%
639 removal of BPB after 3h of UV irradiation. The outstanding photocatalytic
640 performance of TiO₂-AC₂ composite can be attributed to the synergic interaction
641 between activated PBS transformed to carbon during thermal treatment and TiO₂ as
642 confirmed by Raman analysis presented earlier. As a conclusion, phosphoric
643 chemical activation of PBS is beneficial for photocatalytic activity of *piliostigma* based
644 composite. For this reason, TiO₂-AC₂ composite is chosen for further experiments.

645

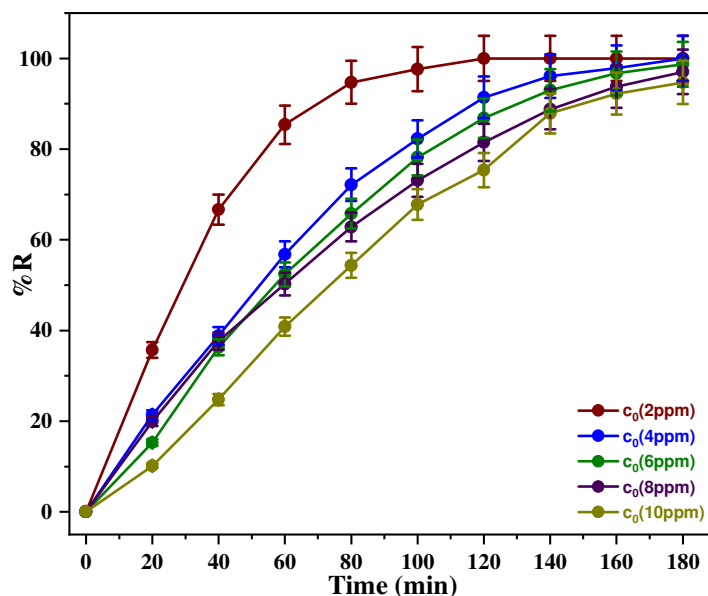


646

647 **Fig.13.** (a) Adsorption-desorption equilibrium test, (b) Photodegradation of BPB
 648 under UV light irradiation by all photocatalyst (C=6ppm; m=150mg; V=500mL; pH
 649 natural)

650 **3.5.1. Effect of concentrations and kinetics study**

651 To get insight into the mechanisms that affect the photocatalytic efficiency of the
 652 TiO₂-AC₂ composite towards the BPB dye molecules, the pollutant concentration, a
 653 very important parameter in waste water treatment, needs to be monitored and
 654 studied. [103]. The effect of initial BPB dye concentrations on the photocatalytic
 655 elimination has been varied from 2 ppm to 10 ppm at natural pH and a catalyst dose
 656 of 200 mg/L. As depicted in Fig. 14., the removal % of BPB dye is inversely
 657 decreasing with the increase of pollutant concentrations. This decrease in
 658 degradation efficiency might be caused by the presence of increased dye molecule in
 659 the solution compared to the number of SO₄⁻ and OH⁻ radicals [31]. A high initial
 660 concentration can decrease the level of reaction between BPB dye and reactive
 661 species. Furthermore, reactive free radicals might have been consumed by the
 662 intermediates causing competitive parallel reactions between free radicals and BPB
 663 dye molecules and intermediates [31]. On the other hand, higher BPB concentrations
 664 revealed strong absorption of light, consequently limiting the generation of higher
 665 concentrations of reactive oxygen species (ROS) and the diffusion step of the photo-
 666 excited to the TiO₂-AC₂ surface [29]. Similar results have been reported by other
 667 works on the photocatalytic degradation of BPB dye [102,103], Reactive Green 12
 668 dye [29], Sudan Black B dye [31].



669

670 **Fig. 14.** Effect of BPB dye initial concentrations ($m=150\text{mg}$; $V=500\text{mL}$; pH natural)

671 Concerning the kinetics of the studied system, the experimental data was fitted to
 672 pseudo first order [104,105] and Langmuir-Hinshelwood model [30] according to Eqs.
 673 (5) and (6):

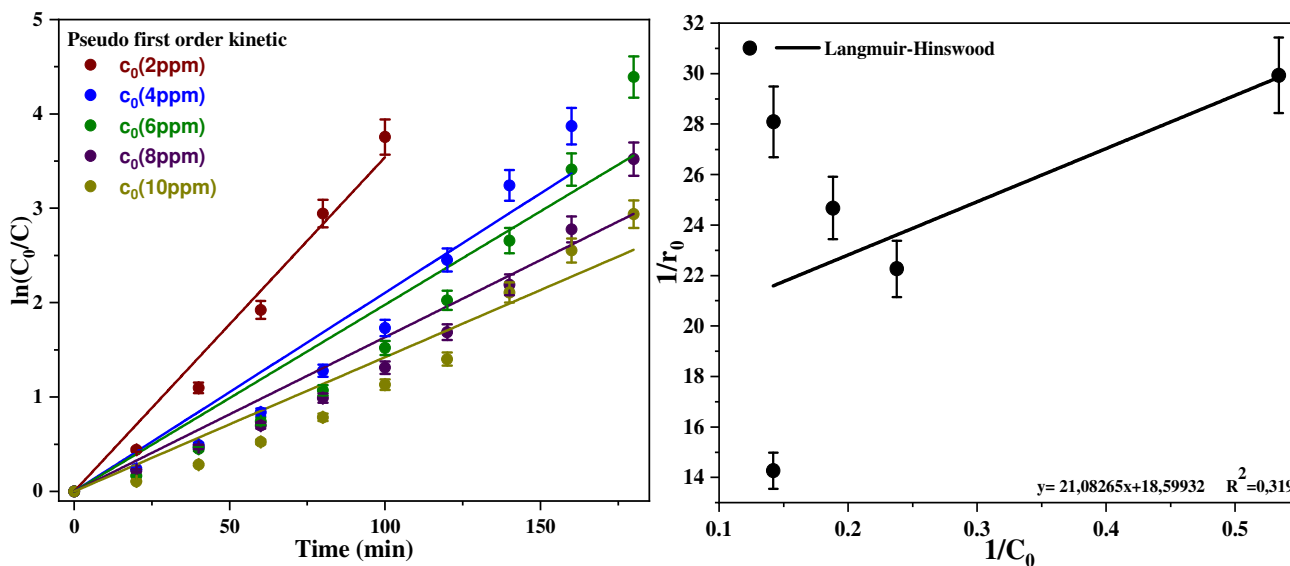
674
$$\ln\left(\frac{C_0}{C}\right) = K_{app} \cdot t \quad (5)$$

675
$$\frac{1}{r_0} = \frac{1}{k} + \frac{1}{kK} \frac{1}{C_0} \quad (6)$$

676 where C_0 and C represents the initial and actual concentration at time t respectively,
 677 K_{app} the apparent rate constant, r_0 is the initial rate of disappearance, k denotes the
 678 reaction rate constant for the process and K is the adsorption coefficient of reactants.

679 The plots and calculated kinetic parameters allow to understand the photocatalytic
 680 activity of the synthesised biomass based photocatalyst [106]. Fig. 15. demonstrates
 681 that the data was well-fitted with pseudo-first order kinetic model [107] with a
 682 correlation coefficient value of R^2 between 0.96 to 0.99 (Table 15) for both
 683 concentrations while the data does not fit the Langmuir-Hinshelwood model. The
 684 degradation rate constant as summarised in Table 15 shows that the rates inversely
 685 decrease with the increase of the contaminant concentration. It can be observed that
 686 the prepared $\text{TiO}_2\text{-AC}_2$ composite exhibits highest degradation rate when the initial
 687 concentration is low. As displayed in Fig. 15., the Langmuir-Hinshelwood model was
 688 not appropriate to describe the heterogenous degradation of the BPB molecules dye.

689 The degradation efficiency of the TiO₂-AC₂ composite is related to the synergy of
 690 biomass and TiO₂. Similar results to this trend are observed from literature by [107–
 691 110], [29].



692
 693 **Fig. 15.** Pseudo first order kinetic and Langmuir-Hinshelwood model.

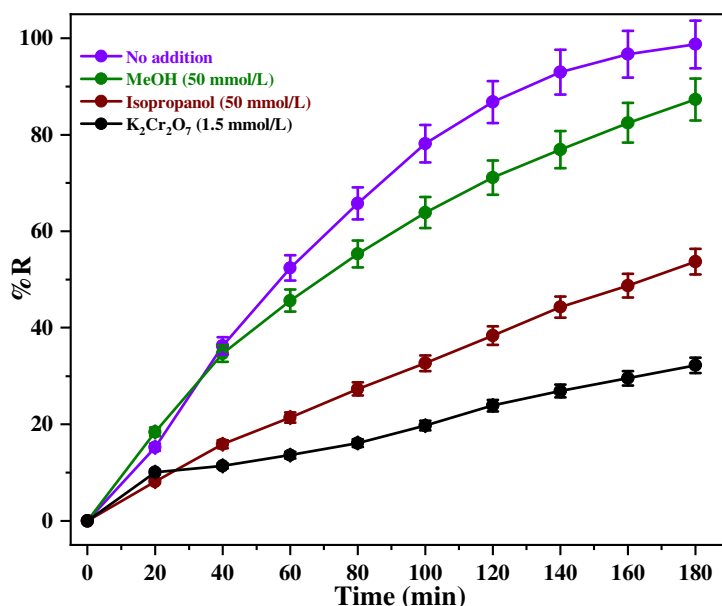
694 **Table 15** kinetic parameters

$C_0(\text{mg/L})$	$K_{\text{app}}(\text{min}^{-1})$	R^2	$t_{1/2}$
2	0.035	0.99	19.56
4	0.021	0.97	32.92
6	0.019	0.96	35.04
8	0.016	0.97	42.42
10	0.014	0.96	48.74

695
 696 **3.5.2. Implication of the contribution of reactive oxygen species (ROS)**

697 To illustrate the potential degradation behaviour of TiO₂-AC₂ composite, a scavenging
 698 study was performed to identify the dominant reactive oxidising species ($\text{HO}\cdot$, $\text{O}_2^{\cdot-}$, h^+)
 699 involved in the photocatalytic medium. The three primary selective scavengers used
 700 to evaluate the inhibition effect are MeOH for electronic holes, iso-propanol for $\text{HO}\cdot$
 701 and potassium dichromate for $\text{O}_2^{\cdot-}$ [30]. As displayed in Fig. 16., the inhibition effect
 702 followed the order $\text{O}_2^{\cdot-} > \text{HO}\cdot > h^+$. The $\text{O}_2^{\cdot-}$ were identified as the key reactive species
 703 responsible for the degradation of BPB dye since the removal yields was significantly
 704 quenched from 100% to 32.19% by potassium dichromate scavenger. The slight

705 inhibition exerted by isopropanol and MeOH scavengers on the degradation of BPB
 706 revealed that both HO· and h^+ radicals played a secondary role in the photocatalytic
 707 reaction process.



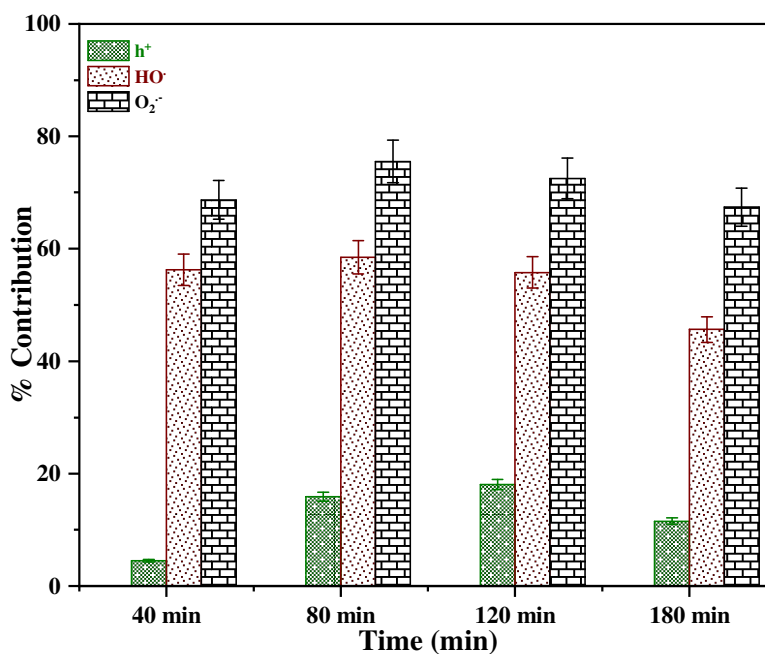
708

709 **Fig. 16.** Effect of different scavengers on the elimination of BPB by TiO₂-AC₂
 710 (C=6ppm; m=150mg; V=500mL; pH natural)

711 On the other hand, Fig. 17. depicts the contribution % of each radical involved in the
 712 photocatalytic reaction for a wide time range. O₂^{•-} radical have significant contribution
 713 % followed by HO·. The holes (h^+) present a contribution less than 20%. The sum of
 714 various contribution adds up to more than 100% due to the fact that there are some
 715 intermediate reactions that contribute to the conversion of one radical to another as
 716 assumed by the following reactions [111–113], [30],:

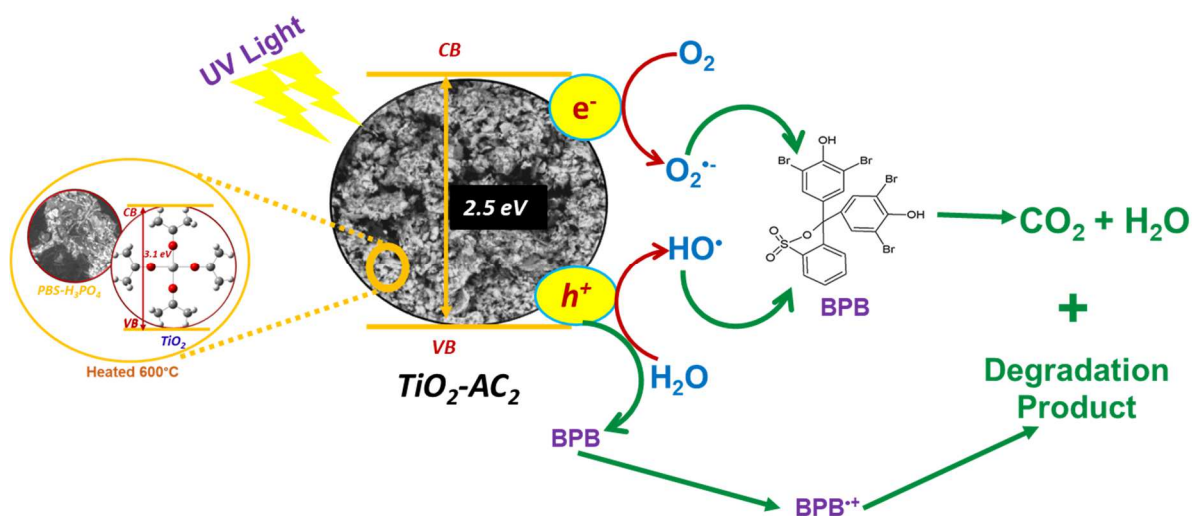


726 It can be observed from reaction (2) and (4) that the holes in the presence of
 727 hydroxide ions and $O_2^{\cdot -}$ in the presence of protons recombine to H_2O_2 (reaction 8),
 728 which leads to HO^{\cdot} radical in the medium by homolytic break up (reaction 9). In
 729 general, the photoactive catalyst produces reactive oxygen species (HO^{\cdot} , $O_2^{\cdot -}$, h^+)
 730 [114].



731
 732 **Fig. 17.** Radicals' contribution during the elimination of BPB by TiO₂-AC₂

733 The possible BPB degradation mechanism onto TiO₂-AC₂ composite is explained in
 734 the pictorial representation as shown is Scheme B below. As demonstrated earlier,
 735 $O_2^{\cdot -}$, HO^{\cdot} and h^+ generated radicals played an important role in the photocatalytic
 736 degradation of BPB.



738 **Scheme B:** A pictorial of possible photocatalytic mechanism for degradation of BPB
739 by piliostigma based composite

740 **3.5.3. Experimental design results**

741 Design of experiments is a systematic approach for distinguishing the importance of
742 certain process variables on the process outputs, their interactions and for controlling
743 them towards optimum response [115]. To determine the relationship between a set
744 of adjustable experimental parameters and obtained results, an empirical modelling
745 technique known as one of the most powerful method for multivariate optimisation
746 towards minimum number of experiments applied, is Response surface methodology
747 (RSM) [116]. This method was employed to analyse and optimise the BPB
748 photocatalytic degradation by TiO₂-AC₂. The design experiment method is typically
749 applied to study the influence of various factors and to construct the data-driven
750 models that are relevant for process optimisation [117]. In this regard, RSM-BBD was
751 performed with 13 runs for the surface models describing the degradation removal %,
752 with the results given in Table 16. The degradation efficiency ranges from 26.69 to
753 100%.

754 **Table 16** Experimental run table and response

Run	A: Catalyst Dose (mg)	B: pH	C: NaCl Concentration (mg/L)	Response : Degradation (%)
1	300	3	15	100
2	400	7	15	77.99
3	200	11	10	26.7
4	400	3	10	100
5	200	7	5	65.82
6	300	11	5	26.69
7	200	3	10	100
8	300	3	5	100
9	400	11	10	25.43
10	200	7	15	36.52
11	300	11	15	31.22
12	300	7	10	49.52
13	400	7	5	41.56

755

756 To validate the model, an analysis of variance (ANOVA) was applied, the results are
 757 presented in Table 17. The statistical significance of the model is assigned as the F-
 758 value [118]. The F-value of 586.4 implies that the model is highly significant. There is
 759 only a 0.01% chance that the F-value with this magnitude could occur due to noise
 760 [119], [37]. A very low probability value (P-value < 0.0017) confirms that the model is
 761 strongly significant over the 95% confidence level term. According to Sohrabi,
 762 Shahnaz, a model is significant when the P-value is <0.05 [118], [98]. The non-
 763 significance of lack of fit is favourable and specifies the high predictability of the
 764 model.

765 **Table 17** ANOVA table and degree of fit

Source	Sum of Square	Degree of Freedom	Mean Square	F-Value	P-Value
Model	0.7378	10	0.0738	586.4	0.0017
A	0.0045	1	0.0045	35.42	0.0271
B	0.3509	1	0.3509	2788.83	0.0004
C	0.001	1	0.001	7.59	0.1104
AB	0.0001	1	0.0001	0.6955	0.4921
AC	0.0728	1	0.0728	578.25	0.0017
BC	0.0009	1	0.0009	7.5	0.1115
B ²	0.0016	1	0.0016	12.83	0.0699
C ²	0.0016	1	0.0016	12.43	0.0719
AB ²	0.0029	1	0.0029	23.02	0.0408
BC ²	0.0008	1	0.0008	6.33	0.1282
Residual	0.0003	2	0.0001		
Cor Total	0.7381	12			
	R²	0.9997			
	Adjusted-R²	0.9980			
Degree of fit	Predicted-R²	0.9758			
	Adeq		59.1020		
	Precision				

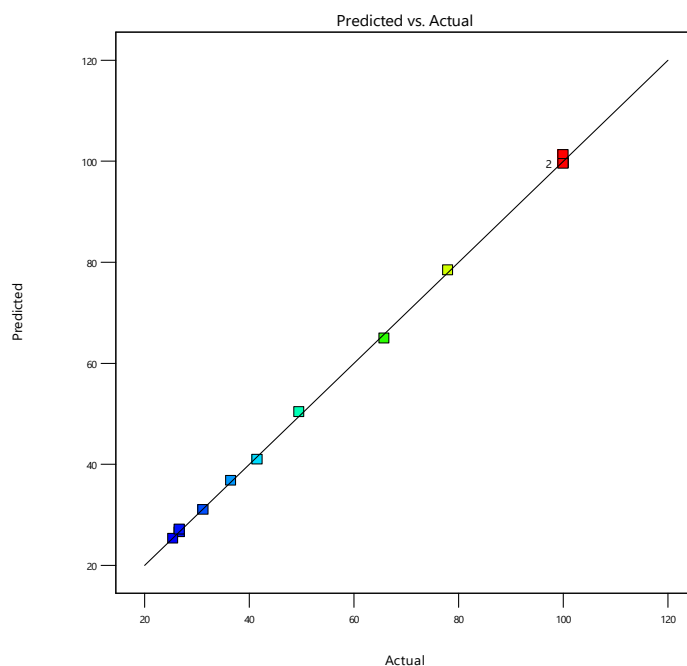
766

767 Based on the experimental design data shown on Table 17, a polyfunctional model
 768 equation that describes the photodegradation process was established, expressed as
 769 follows (Eq. (7)):

$$\begin{aligned}
 770 \text{ (%Degradation)}^{0.2} = & +3.80260 - 0.003447 * A_{\text{catalyst}} - 0.179172 * B_{\text{pH}} - 0.075070 * C_{\text{NaCl}} + \\
 771 & 0.000321 * A_{\text{catalyst}} * B_{\text{pH}} + 0.000270 * A_{\text{catalyst}} * C_{\text{NaCl}} - 0.003225 * B_{\text{pH}} * C_{\text{NaCl}} + 0.008637 * B_{\text{pH}}^2 - \\
 772 & 0.000452 * C_{\text{NaCl}}^2 - 0.000024 * A_{\text{catalyst}} * B_{\text{pH}}^2 + 0.000200 * B_{\text{pH}} * C_{\text{NaCl}}^2 \quad (7)
 \end{aligned}$$

773 This empirical linear regression (Eq. (7)) provides clear information about the positive
 774 or negative effect of the main variables while the numerical coefficient related to the
 775 magnitude/significance of the effect. It is obvious from Eq. (7) that the pH plays the
 776 most significant role in the process followed by the catalyst dose. The NaCl
 777 concentration had a much smaller and symmetrical proportional effect depending on
 778 the catalyst dose.

779 The values of the R^2 , adjusted- R^2 and predicted R^2 coefficients of the applied BBD
 780 model were 0.9997, 0.9980 and 0.9758 respectively (Table 17). These R^2 values
 781 correspond to the level of agreement between degradation % values obtained
 782 experimentally and those predicted by the proposed model as implemented in Fig.
 783 18. The adequate precision, which measures the signal to noise ratio, is 59.102,
 784 much greater than the lowest acceptable value of 4. This practically means that the
 785 proposed model can be reliably used to navigate the design area, within the limit of
 786 variables determined earlier (Table 3).



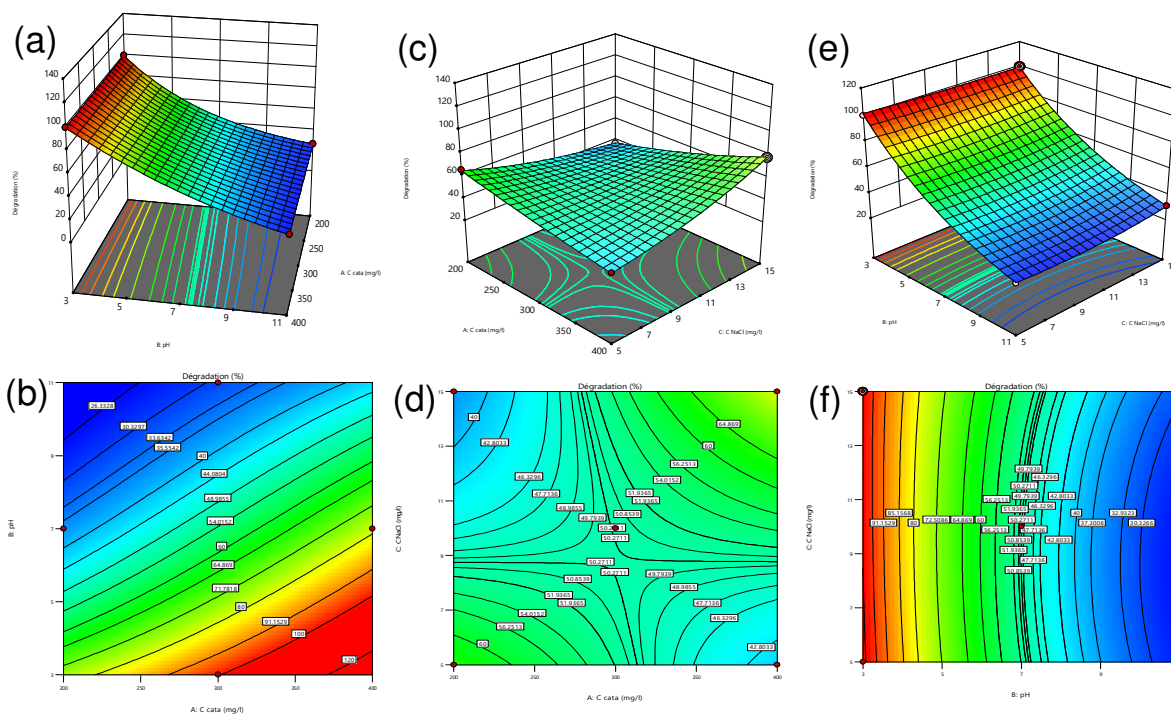
787

788 **Fig. 18.** Correlation between the actual and the predicted values of degradation yield

789 **3.5.4. Response surface analysis**

790 Three dimensional surfaces and contour plots are graphical representations of the
791 regression equation for the optimisation of the reaction conditions, they are a very
792 useful approach in revealing the factors that affect the reaction system. The results
793 obtained from the combined interaction between three variables are depicted in Fig.
794 19.

795 Fig. 19 (a and b). shows the simultaneous influence of catalyst dose and pH of
796 solution on photodegradation of BPB dye. As can be seen in the plots, the interaction
797 effect of pH value and catalyst dose on the elimination of BPB reveals an exponential
798 response surface. Furthermore, the combined effect of factors suggested that the
799 high catalyst dose (300 mg/L) and low pH (3) are suitable for BPB degradation by
800 $\text{TiO}_2\text{-AC}_2$. The corresponding contour plot (Fig. 19 (b).) was applied to facilitate a
801 better understanding of the information related to the interaction effect of factors on
802 the response. The darker red region of the plot indicates maximum % degradation
803 (response). Fig. 19 (c and d). shows the combined effect of the catalyst dose and the
804 interference of NaCl salt. It is evident that the removal percent of BPB degradation
805 shows symmetric response surface. The photodegradation % is high at low catalyst
806 dose and low NaCl concentrations while it remains at high values at increased
807 catalyst dose and NaCl concentrations. This result revealed that the response is
808 proportional to the catalyst dose and the NaCl concentration in the medium. The
809 relating contour plot (Fig. 19 (d).) gives more visibility of the factors that influence on
810 the response. The green area of the contour corresponds to high % removal.
811 Concerning the combined effect of pH and NaCl as depicted in Fig. 19 (e and f). on
812 the photodegradation of BPB, the response increases with the decrease of pH from
813 11 to 3 and the NaCl salt does not affect the degradation process. The maximum %
814 removal was observed at pH 3 as shown earlier. The corresponding contour plot (Fig.
815 19 (f).) establishes that regardless of the amount of NaCl concentration, the highest
816 value of response is still remains at pH 3.



817

818 **Fig. 19.** Response surface and contour plots showing simultaneous influence of
819 factors

820 The photocatalytic activity of the composite was compared with other photocatalysts
821 previously applied for the degradation of BPB dye, summarised in table 18. Despite
822 the difference of operating conditions, the synthesised composite in this study
823 achieved 100% of BPB elimination. The removal % is higher than PC500 with similar
824 dye concentration.

825 **Table 18** Comparative table of operational conditions and elimination efficiency for
826 BPB by other alternative adsorbents.

Catalyst	Irradiation time (min)	pH	Concentration (mg/L) /volume (mL)	Catalyst dose (g)	Efficiency (%)	References
PC500	100	6.3	10 /50	1	80	[103]
TiO ₂ -sap	120	10	20/500	0.2	50	[108]
ZnO-Nb ₂ O ₅	120	5	6/50	0.2	79	[110]
Pth-GNPs(50)	60	3	20/100	0.05	94.1	[120]
HNPs/TUD-1	60	-	30/500	0.2	96.7	[104]
MNPs	60	-	20/500	0.2	89.09	[121]
TiO ₂ -AC ₂	180	4.3	10/500	0.015	100	Present study

827

828 4. Conclusions

829 Being a low value and abundantly available wild bio-waste, *piliostigma reticulatum*
830 fruits can be valorised as a sustainable and environmentally friendly biomass for low
831 cost, easy and feasible synthesis of biobased composite materials applied for
832 wastewater treatment. *Piliostigma* decorated TiO_2 composites were efficient in the
833 removal of Cr(VI) as successfully demonstrated by adsorption experiments and
834 characterisation techniques that provided information on organic and inorganic
835 composition (FTIR, XRS-FP), morphology (SEM) and crystallographic view (XRD) of
836 the materials. The obtained material through the second synthesis process (TiO_2 -
837 AC_2) exhibited high photocatalytic performance towards BPB dye; the optimisation
838 parameters obtained by RSM gives a better understanding of combined effect of
839 factors in the reaction system for the optimum use of photodegradation process. The
840 best adsorption removal results obtained from key operational parameters were at pH
841 1.5 with 0.01g of each composite and Cr(VI) concentration of 2 mg/L for a contact
842 time of 30 min. The pseudo-second order kinetic fitted best the experimental data at
843 equilibrium time with an uptake capacity similar to the calculated value ($q_{\text{exp}} = 1.93$
844 mg/g; 1.86 mg/g and $q_{\text{ecal}} = 1.92$ mg/g; 1.86 mg/g) and higher correlation coefficient
845 ($R^2 = 0.99$). The Sips and Marczewski-Jaroniec equilibrium isotherm fitted adequately
846 the experimental results of which adsorption maxima are 3.46 mg/g; 3.49 mg/g
847 compared to 3.25 mg/g; 3.53 mg/g. These results revealed that, the interaction
848 between the composites and Cr(VI) follows chemisorption process as can be inferred
849 from the low contact time. Optimisation through response surface methodology
850 indicated that the pH of solution was the most influential factor, whereas catalyst
851 dosage and NaCl salt interference had a much lower effect when performing
852 photodegradation of BPB dye. The analysis of variance from BBD showed good
853 statistical results and provided a significant model for the reaction system. It was
854 demonstrated that an abundant biowaste, such as *piliostigma reticulatum* fruits can
855 be transformed to a high added value material by a simple and cost-efficient
856 synthesis process. *Piliostigma* based composite presents a satisfactory performance
857 toward removal of Cr(VI) by adsorption and BPB dye by photocatalysis. This study
858 revealed an efficient material for the removal of both organic and inorganic
859 contaminants from a wastewater. Therefore, its characteristics and qualities make it a

860 suitable adsorbent implemented on wastewater treatment for the removal of
861 contaminants.

862 **Author contributions:** Conceptualisation, S.M., S.D., H.M. A.K and H.Z.;
863 Methodology, S.M., H.Z., S.D., P.B, H.M., A.K, A.M. and L.F.; Software, S.M. and
864 H.Z.; Validation, H.Z., S.D., H.M., and A.K.; Formal Analysis, D.O.O. and P.B.;
865 Investigation, S.M., H.Z., L.F and S.D.; Data curation, S.M. and H.Z.; Writing-original
866 draft preparation, S.M.; Writing-review and editing, S.M., H.Z., L.F., A.M., P.B., S.D.,
867 A.K., D.O.O.; Visualisation, A.K., H.Z., S.D., H.M. and P.B.; Supervision, H.Z., A.K.,
868 A.M., L.F., P.B. and S.D. All authors have read and agreed to published version of
869 the manuscript.

870 **Funding:** This research received no external funding

871 **Data Availability Statement:** Not Applicable

872 **Acknowledgment:** The authors would like to thank Ivane LELIEVRE (UniLaSalle
873 Rennes) for their technical help. Authors thank Lawrence FREZET from “ICCF” for
874 BET measurements. The authors would like to acknowledge the Erasmus+
875 International Credit Mobility for the Grant (Grant agreement number: 2019-1-FR01-
876 KA107-060920) between Unilasalle Polytechnic Institute and University of Maroua.

877 **Conflict of interest:** The authors declare that they have no known competing
878 financial interests or personal relationships that could have appeared to influence the
879 trend reported in this paper.

880 **References**

881

882 [1] P. Szoldra, M. Frąc, W. Pichór, Effect of sol composition on the properties of
883 TiO₂ powders obtained by the sol-gel method, Powder Technol. 387 (2021)
884 261–269. <https://doi.org/10.1016/j.powtec.2021.04.037>.

885 [2] A.A. El-Zahhar, N.S. Awwad, E.E. El-Katori, Removal of bromophenol blue dye
886 from industrial waste water by synthesizing polymer-clay composite, J. Mol.
887 Liq. 199 (2014) 454–461. <https://doi.org/10.1016/j.molliq.2014.07.034>.

888 [3] C. Patra, E. Suganya, S. Sivaprakasam, G. Krishnamoorthy, S.
889 Narayanasamy, A detailed insight on fabricated porous chitosan in eliminating
890 synthetic anionic dyes from single and multi-adsorptive systems with related
891 studies, Chemosphere. 281 (2021) 130706.

- 892 <https://doi.org/10.1016/j.chemosphere.2021.130706>.
- 893 [4] A. Srivastava, L. Kumar, S. Kumar, R. Rani, Heliyon Microbial decolorization of
894 Reactive Black 5 dye by *Bacillus albus* DD1 isolated from textile water ef fl
895 uent : kinetic , thermodynamics & decolorization mechanism, Heliyon. 7 (2022)
896 e08834. <https://doi.org/10.1016/j.heliyon.2022.e08834>.
- 897 [5] H. Mazaheri, M. Ghaedi, A. Asfaram, S. Hajati, Performance of CuS
898 nanoparticle loaded on activated carbon in the adsorption of methylene blue
899 and bromophenol blue dyes in binary aqueous solutions: Using ultrasound
900 power and optimization by central composite design, J. Mol. Liq. 219 (2016)
901 667–676. <https://doi.org/10.1016/j.molliq.2016.03.050>.
- 902 [6] S. Naraginti, Y.C. Yong, Enhanced detoxification of p-bromophenol by novel
903 Zr/Ag-TiO₂@rGO ternary composite: Degradation kinetics and phytotoxicity
904 evolution studies, Ecotoxicol. Environ. Saf. 170 (2019) 355–362.
905 <https://doi.org/10.1016/j.ecoenv.2018.12.001>.
- 906 [7] K.G. Akpomie, J. Conradie, Efficient synthesis of magnetic nanoparticle-Musa
907 acuminata peel composite for the adsorption of anionic dye, Arab. J. Chem. 13
908 (2020) 7115–7131. <https://doi.org/10.1016/j.arabjc.2020.07.017>.
- 909 [8] T. Sansenya, N. Masri, T. Chankhanittha, T. Senasu, J. Piriyanon, S.
910 Mukdasai, S. Nanan, Hydrothermal synthesis of ZnO photocatalyst for
911 detoxification of anionic azo dyes and antibiotic, J. Phys. Chem. Solids. 160
912 (2022) 110353. <https://doi.org/10.1016/j.jpics.2021.110353>.
- 913 [9] K. Alamelu, B.M. Jaffar Ali, Au nanoparticles decorated sulfonated graphene-
914 TiO₂ nanocomposite for sunlight driven photocatalytic degradation of
915 recalcitrant compound, Sol. Energy. 211 (2020) 1194–1205.
916 <https://doi.org/10.1016/j.solener.2020.10.058>.
- 917 [10] S. Alahiane, A. Sennaoui, F. Sakr, M. Dinne, S. Qourzal, A. Assabbane,
918 Synchronous role of coupled adsorption-photocatalytic degradation of Direct
919 Red 80 with nanocrystalline TiO₂-coated non-woven fibres materials in a static
920 batch photoreactor, Groundw. Sustain. Dev. 11 (2020) 100396.
921 <https://doi.org/10.1016/j.gsd.2020.100396>.
- 922 [11] Y. Xiang, M. Gao, T. Shen, G. Cao, B. Zhao, S. Guo, Comparative study of

- 923 three novel organo-clays modified with imidazolium-based gemini surfactant on
924 adsorption for bromophenol blue, *J. Mol. Liq.* 286 (2019) 110928.
925 <https://doi.org/10.1016/j.molliq.2019.110928>.
- 926 [12] M.H. Mondal, W. Begum, M. Nasrollahzadeh, F. Ghorbannezhad, A
927 comprehensive review on chromium chemistry along with detection , speciation
928 , extraction and remediation of hexavalent chromium in contemporary science
929 and technology, 59 (2021) 711–732. <https://doi.org/10.1002/vjch.202100048>.
- 930 [13] P. Prema, V. Nguyen, K. Venkatachalam, J.M. Murugan, H.M. Ali, M.Z.M.
931 Salem, B. Ravindran, P. Balaji, Hexavalent chromium removal from aqueous
932 solutions using biogenic iron nanoparticles : Kinetics and equilibrium study,
933 *Environ. Res.* 205 (2022) 112477.
934 <https://doi.org/10.1016/j.envres.2021.112477>.
- 935 [14] S. Mouhamadou, S. Dalhatou, N. Dobe, R. Djakba, O.O. Fasanya, Linear and
936 Non - linear Modelling of Kinetics and Equilibrium Data for Cr (VI) Adsorption
937 by Activated Carbon Prepared from *Piliostigma reticulatum*, *Chem. Africa.*
938 (2022). <https://doi.org/10.1007/s42250-022-00324-5>.
- 939 [15] P. Karthikeyan, S.S.D. Elanchezhiyan, H. Ali, T. Banu, M.H. Farzana, C. Min,
940 Chemosphere Hydrothermal synthesis of hydroxyapatite-reduced graphene
941 oxide (1D e 2D) hybrids with enhanced selective adsorption properties for
942 methyl orange and hexavalent chromium from aqueous solutions,
943 *Chemosphere.* 276 (2021) 130200.
944 <https://doi.org/10.1016/j.chemosphere.2021.130200>.
- 945 [16] Y. Zhan, S. He, X. Wan, J. Zhang, B. Liu, J. Wang, Z. Li, *Journal of Colloid and*
946 *Interface Science* Easy-handling bamboo-like polypyrrole nanofibrous mats
947 with high adsorption capacity for hexavalent chromium removal, *J. Colloid*
948 *Interface Sci.* 529 (2018) 385–395. <https://doi.org/10.1016/j.jcis.2018.06.033>.
- 949 [17] J. Chen, Y. Pu, C. Wang, J. Han, Y. Zhong, K. Liu, Synthesis of a novel
950 nanosilica-supported poly β -cyclodextrin sorbent and its properties for the
951 removal of dyes from aqueous solution, *Colloids Surfaces A Physicochem.*
952 *Eng. Asp.* 538 (2018) 808–817. <https://doi.org/10.1016/j.colsurfa.2017.11.048>.
- 953 [18] S. Mishra, S.S. Sahoo, A.K. Debnath, K.P. Muthe, N. Das, P. Parhi, Cobalt

- 954 ferrite nanoparticles prepared by microwave hydrothermal synthesis and
955 adsorption efficiency for organic dyes: Isotherms, thermodynamics and kinetic
956 studies, *Adv. Powder Technol.* 31 (2020) 4552–4562.
957 <https://doi.org/10.1016/j.appt.2020.10.001>.
- 958 [19] A.S. Shair, A.S.A. Dena, I.M. El-Sherbiny, Matrix-dispersed PEI-coated
959 SPIONs for fast and efficient removal of anionic dyes from textile wastewater
960 samples: Applications to triphenylmethanes, *Spectrochim. Acta - Part A Mol.*
961 *Biomol. Spectrosc.* 249 (2021) 119301.
962 <https://doi.org/10.1016/j.saa.2020.119301>.
- 963 [20] I. Fatimah, E. Zunita Pratiwi, W. Prio Wicaksono, Synthesis of magnetic
964 nanoparticles using *Parkia speciosa* Hassk pod extract and photocatalytic
965 activity for Bromophenol blue degradation, *Egypt. J. Aquat. Res.* 46 (2020) 35–
966 40. <https://doi.org/10.1016/j.ejar.2020.01.001>.
- 967 [21] S. Behnam, M. Kazemeini, N. Mohammad, A study of the DR23 dye
968 photocatalytic degradation utilizing a magnetic hybrid nanocomposite of MIL-53
969 (Fe)/ CoFe₂O₄ : Facile synthesis and kinetic investigations, *J. Mol. Liq.* 301
970 (2020) 112427. <https://doi.org/10.1016/j.molliq.2019.112427>.
- 971 [22] A.C. Khorasani, S.A. Shojaosadati, Magnetic pectin-*Chlorella vulgaris*
972 biosorbent for the adsorption of dyes, *J. Environ. Chem. Eng.* 7 (2019) 103062.
973 <https://doi.org/10.1016/j.jece.2019.103062>.
- 974 [23] W. Xiao, X. Jiang, X. Liu, W. Zhou, Z.N. Garba, I. Lawan, L. Wang, Z. Yuan,
975 Adsorption of organic dyes from wastewater by metal-doped porous carbon
976 materials, *J. Clean. Prod.* 284 (2021) 124773.
977 <https://doi.org/10.1016/j.jclepro.2020.124773>.
- 978 [24] H. Massai, D. Raphael, M. Sali, Adsorption of Copper Ions (Cu⁺⁺) in
979 Aqueous Solution Using Activated Carbon and Biosorbent from Indian Jujube (*Ziziphus mauritiana*)
980 Seed Hulls, 29 (2020) 13–24.
981 <https://doi.org/10.9734/CSJI/2020/v29i530177>.
- 982 [25] S. Kocaman, Removal of methylene blue dye from aqueous solutions by
983 adsorption on levulinic acid-modified natural shells, *Int. J. Phytoremediation.* 22
984 (2020) 885–895. <https://doi.org/10.1080/15226514.2020.1736512>.

- 985 [26] W.R. Abd-ellatif, N.G. Mahmoud, A.A. Hashem, E.M. Ezzo, S.A. Mahmoud,
986 Jou rna IP, Environ. Technol. Innov. (2022) 102393.
987 <https://doi.org/10.1016/j.eti.2022.102393>.
- 988 [27] I. Ould Brahim, M. Belmedani, H. Hadoun, A. Belgacem, The photocatalytic
989 degradation kinetics of food dye in aqueous solution under UV/ZnO system,
990 React. Kinet. Mech. Catal. 133 (2021) 1075–1095.
991 <https://doi.org/10.1007/s11144-021-02006-8>.
- 992 [28] J. Zhao, L. Yu, H. Ma, F. Zhou, K. Yang, G. Wu, Journal of Colloid and
993 Interface Science Corn stalk-based activated carbon synthesized by a novel
994 activation method for high-performance adsorption of hexavalent chromium in
995 aqueous solutions, J. Colloid Interface Sci. 578 (2020) 650–659.
996 <https://doi.org/10.1016/j.jcis.2020.06.031>.
- 997 [29] H. Zeghioud, N. Khellaf, A. Amrane, H. Djelal, W. Elfalleh, A.A. Assadi, S.
998 Rtimi, Photocatalytic performance of TiO₂ impregnated polyester for the
999 degradation of Reactive Green 12: Implications of the surface pretreatment and
1000 the microstructure, J. Photochem. Photobiol. A Chem. 346 (2017) 493–501.
1001 <https://doi.org/10.1016/j.jphotochem.2017.07.005>.
- 1002 [30] H. Zeghioud, A.A. Assadi, N. Khellaf, H. Djelal, A. Amrane, S. Rtimi,
1003 Photocatalytic performance of Cu x O/TiO₂ deposited by HiPIMS on polyester
1004 under visible light LEDs: Oxidants, ions effect, and reactive oxygen species
1005 investigation, Materials (Basel). 12 (2019).
1006 <https://doi.org/10.3390/ma12030412>.
- 1007 [31] S.B. Shuchi, B.K. Suhan, S. Bin Humayun, M.E. Haque, S. Islam, Journal of
1008 Water Process Engineering Heat-activated potassium persulfate treatment of
1009 Sudan Black B dye : Degradation kinetic and thermodynamic studies, J. Water
1010 Process Eng. 39 (2021) 101690. <https://doi.org/10.1016/j.jwpe.2020.101690>.
- 1011 [32] T. Saeed, A. Naeem, I. Ud, M. Farooq, I. Wali, M. Hamayun, T. Malik,
1012 Synthesis of chitosan composite of metal-organic framework for the adsorption
1013 of dyes ; kinetic and thermodynamic approach, J. Hazard. Mater. 427 (2022)
1014 127902. <https://doi.org/10.1016/j.jhazmat.2021.127902>.
- 1015 [33] F. Anjum, A.M. Asiri, M. Ali, M.I. Khan, S. Bahadar, K. Akhtar, E.M. Bakhsh,

- 1016 K.A. Alamry, S. Yahya, S. Chakraborty, Photo-degradation , thermodynamic
1017 and kinetic study of carcinogenic dyes via zinc oxide / graphene oxide
1018 nanocomposites, *J. Mater. Res. Technol.* 15 (2021) 3171–3191.
1019 <https://doi.org/10.1016/j.jmrt.2021.09.086>.
- 1020 [34] Z.H. Mahmoud, R.A. Al-bayati, A.A. Khadom, The efficacy of samarium loaded
1021 titanium dioxide (Sm : TiO₂) for enhanced photocatalytic removal of
1022 rhodamine B dye in natural sunlight exposure, *J. Mol. Struct.* 1253 (2022)
1023 132267. <https://doi.org/10.1016/j.molstruc.2021.132267>.
- 1024 [35] G. Pereira da Costa, R.A. Rafael, J.C.S. Soares, A.B. Gaspar, Synthesis and
1025 characterization of ZnO-Nb₂O₅ catalysts for photodegradation of bromophenol
1026 blue, *Catal. Today.* 344 (2020) 240–246.
1027 <https://doi.org/10.1016/j.cattod.2019.04.059>.
- 1028 [36] S. De Gisi, G. Lofrano, M. Grassi, M. Notarnicola, Characteristics and
1029 adsorption capacities of low-cost sorbents for wastewater treatment: A review,
1030 *Sustain. Mater. Technol.* 9 (2016) 10–40.
1031 <https://doi.org/10.1016/j.susmat.2016.06.002>.
- 1032 [37] F. Çatlıoğlu, S. Akay, E. Turunç, B. Gözmen, I. Anastopoulos, B. Kayan, D.
1033 Kalderis, Preparation and application of Fe-modified banana peel in the
1034 adsorption of methylene blue: Process optimization using response surface
1035 methodology, *Environ. Nanotechnology, Monit. Manag.* 16 (2021).
1036 <https://doi.org/10.1016/j.enmm.2021.100517>.
- 1037 [38] M.A. Al-Ghouti, D.A. Da'ana, Guidelines for the use and interpretation of
1038 adsorption isotherm models: A review, *J. Hazard. Mater.* 393 (2020) 122383.
1039 <https://doi.org/10.1016/j.jhazmat.2020.122383>.
- 1040 [39] J. Wang, X. Guo, Adsorption isotherm models: Classification, physical
1041 meaning, application and solving method, *Chemosphere.* 258 (2020) 127279.
1042 <https://doi.org/10.1016/j.chemosphere.2020.127279>.
- 1043 [40] H. Nguyen, S. You, A. Hosseini-bandegharai, Mistakes and inconsistencies
1044 regarding adsorption of contaminants from aqueous solutions : A critical review,
1045 *Water Res.* 120 (2017) 88–116. <https://doi.org/10.1016/j.watres.2017.04.014>.
- 1046 [41] R. Ramadoss, D. Subramania, Adsorption of Chromium Using Blue Green

- 1047 Algae-Modeling and Application of Various Isotherms, *Int. J. Chem. Technol.*
1048 10 (2017) 1–22. <https://doi.org/10.3923/ijct.2018.1.22>.
- 1049 [42] B.R. Patra, S. Nanda, A.K. Dalai, V. Meda, Slow pyrolysis of agro-food wastes
1050 and physicochemical characterization of biofuel products, *Chemosphere*. 285
1051 (2021) 131431. <https://doi.org/10.1016/j.chemosphere.2021.131431>.
- 1052 [43] S.S. Sahoo, V.K. Vijay, R. Chandra, H. Kumar, Production and characterization
1053 of biochar produced from slow pyrolysis of pigeon pea stalk and bamboo,
1054 *Clean. Eng. Technol.* 3 (2021) 100101.
1055 <https://doi.org/10.1016/j.clet.2021.100101>.
- 1056 [44] S. Naik, V. V. Goud, P.K. Rout, K. Jacobson, A.K. Dalai, Characterization of
1057 Canadian biomass for alternative renewable biofuel, *Renew. Energy*. 35 (2010)
1058 1624–1631. <https://doi.org/10.1016/j.renene.2009.08.033>.
- 1059 [45] A.S. Alkorbi, H. Muhammad Asif Javed, S. Hussain, S. Latif, M.S. Mahr, M.S.
1060 Mustafa, R. Alsaiani, N.A. Alhemiary, Solar light-driven photocatalytic
1061 degradation of methyl blue by carbon-doped TiO₂ nanoparticles, *Opt. Mater.*
1062 (Amst). 127 (2022) 112259. <https://doi.org/10.1016/j.optmat.2022.112259>.
- 1063 [46] T.T. Loan, N.N. Long, Effect of Co²⁺ doping on Raman spectra and the phase
1064 transformation of TiO₂:Co²⁺ nanowires, *J. Phys. Chem. Solids*. 124 (2019)
1065 336–342. <https://doi.org/10.1016/j.jpcs.2018.09.007>.
- 1066 [47] D. Komaraiah, E. Radha, J. James, N. Kalarikkal, J. Sivakumar, M. V. Ramana
1067 Reddy, R. Sayanna, Effect of particle size and dopant concentration on the
1068 Raman and the photoluminescence spectra of TiO₂:Eu³⁺ nanophosphor thin
1069 films, *J. Lumin.* 211 (2019) 320–333.
1070 <https://doi.org/10.1016/j.jlumin.2019.03.050>.
- 1071 [48] Z. Bian, Y. Feng, H. Li, H. Yu, H. Wu, Adsorption-photocatalytic degradation
1072 and kinetic of sodium isobutyl xanthate using the nitrogen and cerium co-
1073 doping TiO₂-coated activated carbon, *Chemosphere*. 263 (2021) 128254.
1074 <https://doi.org/10.1016/j.chemosphere.2020.128254>.
- 1075 [49] B. Tu, H. Chen, J. Deng, S. Xue, X. Ma, Y. Xu, Z. Xie, H. Tao, Preparation of
1076 N-I co-doped TiO₂ supported on activated carbon photocatalyst for efficient
1077 photocatalytic reduction of Cr(VI) ions, *Colloids Surfaces A Physicochem. Eng.*

- 1078 Asp. 622 (2021) 126660. <https://doi.org/10.1016/j.colsurfa.2021.126660>.
- 1079 [50] K. Trzciński, M. Szkoda, Z. Zarach, M. Sawczak, A.P. Nowak, Towards
1080 spectroscopic monitoring of photoelectrodes: In-situ Raman
1081 photoelectrochemistry of a TiO₂/prussian blue photoanode, *Electrochim. Acta.*
1082 404 (2022) 139774. <https://doi.org/10.1016/j.electacta.2021.139774>.
- 1083 [51] P. Wu, L. Xia, M. Dai, L. Lin, S. Song, Electrosorption of fluoride on TiO₂-
1084 loaded activated carbon in water, *Colloids Surfaces A Physicochem. Eng. Asp.*
1085 502 (2016) 66–73. <https://doi.org/10.1016/j.colsurfa.2016.05.020>.
- 1086 [52] A. Eshaghi, H. Moradi, Optical and photocatalytic properties of the Fe-doped
1087 TiO₂ nanoparticles loaded on the activated carbon, *Adv. Powder Technol.* 29
1088 (2018) 1879–1885. <https://doi.org/10.1016/j.appt.2018.04.026>.
- 1089 [53] C. Orha, R. Pode, F. Manea, C. Lazau, C. Bandas, Titanium dioxide-modified
1090 activated carbon for advanced drinking water treatment, *Process Saf. Environ.*
1091 *Prot.* 108 (2017) 26–33. <https://doi.org/10.1016/j.psep.2016.07.013>.
- 1092 [54] M. Farrag, R. Yahya, Selective solar photocatalytic oxidation of benzyl alcohol
1093 to benzaldehyde over monodispersed Cu nanoclusters/TiO₂/activated carbon
1094 nanocomposite, *J. Photochem. Photobiol. A Chem.* 396 (2020).
1095 <https://doi.org/10.1016/j.jphotochem.2020.112527>.
- 1096 [55] Y.O. Donar, S. Bilge, A. Sinağ, O. Pliekhov, TiO₂/Carbon Materials Derived
1097 from Hydrothermal Carbonization of Waste Biomass: A Highly Efficient, Low-
1098 Cost Visible-Light-Driven Photocatalyst, *ChemCatChem.* 10 (2018) 1134–1139.
1099 <https://doi.org/10.1002/cctc.201701405>.
- 1100 [56] Y. Zhou, Y. Yang, R. Zhao, Z. Chen, J. Lu, Y. Zhang, L. Tan, Y. Shi, In situ
1101 generation of nano TiO₂ on activated carbon fiber with enhanced photocatalytic
1102 degradation performance, *Res. Chem. Intermed.* 47 (2021) 3769–3784.
1103 <https://doi.org/10.1007/s11164-021-04490-y>.
- 1104 [57] X. Feng, X. Li, B. Su, J. Ma, Solid-phase fabrication of TiO₂/Chitosan-biochar
1105 composites with superior UV–vis light driven photocatalytic degradation
1106 performance, *Colloids Surfaces A Physicochem. Eng. Asp.* 648 (2022) 129114.
1107 <https://doi.org/10.1016/j.colsurfa.2022.129114>.
- 1108 [58] H.C. Choi, Y.M. Jung, S. Bin Kim, Size effects in the Raman spectra of TiO₂

- 1109 nanoparticles, *Vib. Spectrosc.* 37 (2005) 33–38.
1110 <https://doi.org/10.1016/j.vibspec.2004.05.006>.
- 1111 [59] G. Chen, J. Chen, Z. Song, C. Srinivasakannan, J. Peng, A new highly efficient
1112 method for the synthesis of rutile TiO₂, *J. Alloys Compd.* 585 (2014) 75–77.
1113 <https://doi.org/10.1016/j.jallcom.2013.09.056>.
- 1114 [60] A.G. Ilie, M. Scarisoareanu, I. Morjan, E. Dutu, M. Badiceanu, I. Mihailescu,
1115 Principal component analysis of Raman spectra for TiO₂ nanoparticle
1116 characterization, *Appl. Surf. Sci.* 417 (2017) 93–103.
1117 <https://doi.org/10.1016/j.apsusc.2017.01.193>.
- 1118 [61] G.K. Sukhadeve, S.Y. Janbandhu, R. Kumar, D.H. Lataye, D.D. Ramteke, R.S.
1119 Gedam, Visible light assisted photocatalytic degradation of Indigo Carmine dye
1120 and NO₂ removal by Fe doped TiO₂ nanoparticles, *Ceram. Int.* (2022).
1121 <https://doi.org/10.1016/j.ceramint.2022.05.053>.
- 1122 [62] N. Zinai, A. Bouzidi, N. Saoula, R. Miloua, M. Medles, W. Filali, E. Garoudja,
1123 Tailoring the structural and optical properties of HiPIMS TiO₂ thin films for
1124 photovoltaic applications, *Opt. Mater. (Amst.)* 131 (2022) 112590.
1125 <https://doi.org/10.1016/j.optmat.2022.112590>.
- 1126 [63] J.J. Jasinski, M. Lubas, K. Suchorab, M. Gawęda, L. Kurpaska, M. Brykala, A.
1127 Kosinska, M. Sitarz, J. Jagielski, Qualitative and semi-quantitative phase
1128 analysis of TiO₂ thin layers by Raman imaging, *J. Mol. Struct.* 1260 (2022).
1129 <https://doi.org/10.1016/j.molstruc.2022.132803>.
- 1130 [64] H. Zeghioud, L. Fryda, H. Djelal, A. Assadi, A. Kane, A comprehensive review
1131 of biochar in removal of organic pollutants from wastewater : Characterization ,
1132 toxicity , activation / functionalization and influencing treatment factors *Journal*
1133 *of Water Process Engineering A comprehensive review of biochar in r, J. Water*
1134 *Process Eng.* 47 (2022) 102801. <https://doi.org/10.1016/j.jwpe.2022.102801>.
- 1135 [65] Z. Zhang, Y. Li, L. Ding, J. Yu, Q. Zhou, Y. Kong, J. Ma, Novel sodium
1136 bicarbonate activation of cassava ethanol sludge derived biochar for removing
1137 tetracycline from aqueous solution: Performance assessment and mechanism
1138 insight, *Bioresour. Technol.* 330 (2021) 124949.
1139 <https://doi.org/10.1016/j.biortech.2021.124949>.

- 1140 [66] N.E. Jasbi, E. Solati, D. Dorrnian, Role of laser fluence in decoration of
1141 graphene nanosheets with TiO₂ nanoparticles by pulsed laser ablation method,
1142 *J. Alloys Compd.* 861 (2021). <https://doi.org/10.1016/j.jallcom.2020.157956>.
- 1143 [67] J.V. Pasikhani, N. Gilani, A.E. Pirbazari, Improvement the wastewater puri fi
1144 cation by TiO₂ nanotube arrays : The e ff ect of etching-step on the photo-
1145 generated charge carriers and photocatalytic activity of anodic TiO₂
1146 nanotubes, 84 (2018) 57–74.
1147 <https://doi.org/10.1016/j.solidstatesciences.2018.08.003>.
- 1148 [68] V.T. Trinh, T.M.P. Nguyen, H.T. Van, L.P. Hoang, T.V. Nguyen, L.T. Ha, X.H.
1149 Vu, T.T. Pham, T.N. Nguyen, N. V. Quang, X.C. Nguyen, Phosphate
1150 Adsorption by Silver Nanoparticles-Loaded Activated Carbon derived from Tea
1151 Residue, *Sci. Rep.* 10 (2020) 1–13. [https://doi.org/10.1038/s41598-020-60542-](https://doi.org/10.1038/s41598-020-60542-0)
1152 [0](https://doi.org/10.1038/s41598-020-60542-0).
- 1153 [69] P.J. Wibawa, M. Nur, M. Asy'ari, H. Nur, SEM, XRD and FTIR analyses of both
1154 ultrasonic and heat generated activated carbon black microstructures, *Heliyon.*
1155 6 (2020) e03546. <https://doi.org/10.1016/j.heliyon.2020.e03546>.
- 1156 [70] R.K. Mishra, K. Mohanty, Pyrolysis of Manilkara zapota seeds over ZSM-5 to
1157 produce high-quality bio-oil and chemicals, *Fuel.* 280 (2020) 118594.
1158 <https://doi.org/10.1016/j.fuel.2020.118594>.
- 1159 [71] Z. Mengting, T.A. Kurniawan, R. Avtar, M.H.D. Othman, T. Ouyang, H. Yujia, Z.
1160 Xueting, T. Setiadi, I. Iswanto, Applicability of TiO₂(B) nanosheets@hydrochar
1161 composites for adsorption of tetracycline (TC) from contaminated water, *J.*
1162 *Hazard. Mater.* 405 (2021). <https://doi.org/10.1016/j.jhazmat.2020.123999>.
- 1163 [72] Q. Luo, G. Li, M. Chen, F. Qin, H. Li, Y. Qiang, Effect Factor of Arsenite and
1164 Arsenate Removal by a Manufactured Material: Activated Carbon-Supported
1165 Nano-TiO₂, *J. Chem.* 2020 (2020). <https://doi.org/10.1155/2020/6724157>.
- 1166 [73] A. Phlayrahan, N. Monarumit, S. Satitkune, P. Wathanakul, Role of Ti Content
1167 on the Occurrence of the 3309-cm⁻¹ Peak in FTIR Absorption Spectra of Ruby
1168 Samples, *J. Appl. Spectrosc.* 85 (2018) 385–390.
1169 <https://doi.org/10.1007/s10812-018-0662-0>.
- 1170 [74] M.E. Azim Araghi, N. Shaban, M. Bahar, Synthesis and characterization of

- 1171 nanocrystalline barium strontium titanate powder by a modified sol-gel
1172 processing, *Mater. Sci. Pol.* 34 (2016) 63–68. [https://doi.org/10.1515/msp-](https://doi.org/10.1515/msp-2016-0020)
1173 2016-0020.
- 1174 [75] A. Sahoo, S. Kumar, K. Mohanty, A comprehensive characterization of non-
1175 edible lignocellulosic biomass to elucidate their biofuel production potential,
1176 *Biomass Convers. Biorefinery.* (2020). [https://doi.org/10.1007/s13399-020-](https://doi.org/10.1007/s13399-020-00924-6)
1177 00924-6.
- 1178 [76] H.M. Oo, P. Karin, N. Chollacoop, K. Hanamura, Physicochemical
1179 characterization of forest and sugarcane leaf combustion's particulate matters
1180 using electron microscopy, EDS, XRD and TGA, *J. Environ. Sci. (China)*. 99
1181 (2021) 296–310. <https://doi.org/10.1016/j.jes.2020.06.036>.
- 1182 [77] S.M.A. El-Gamal, M.S. Amin, M.A. Ahmed, Removal of methyl orange and
1183 bromophenol blue dyes from aqueous solution using Sorel's cement
1184 nanoparticles, *J. Environ. Chem. Eng.* 3 (2015) 1702–1712.
1185 <https://doi.org/10.1016/j.jece.2015.06.022>.
- 1186 [78] S. Sarkar, M. Sarkar, Ultrasound assisted batch operation for the adsorption of
1187 hexavalent chromium onto engineered nanobiocomposite, *Heliyon.* 5 (2019)
1188 1491. <https://doi.org/10.1016/j.heliyon.2019>.
- 1189 [79] X. Liu, Y. Zhang, Y. Liu, T. Zhang, International Journal of Biological
1190 Macromolecules Green method to synthesize magnetic zeolite / chitosan
1191 composites and adsorption of hexavalent chromium from aqueous solutions,
1192 *Int. J. Biol. Macromol.* 194 (2022) 746–754.
1193 <https://doi.org/10.1016/j.ijbiomac.2021.11.121>.
- 1194 [80] A.C.M. Almeida, R.A. do Nascimento, I.C.B. Amador, T.C. de S. Santos, M.C.
1195 Martelli, L.J.G. de Faria, N.F. da P. Ribeiro, Chemically activated red mud:
1196 assessing structural modifications and optimizing adsorption properties for
1197 hexavalent chromium, *Colloids Surfaces A Physicochem. Eng. Asp.* 628
1198 (2021). <https://doi.org/10.1016/j.colsurfa.2021.127325>.
- 1199 [81] I. Enniya, L. Rghioui, A. Jourani, Adsorption of hexavalent chromium in
1200 aqueous solution on activated carbon prepared from apple peels, *Sustain.*
1201 *Chem. Pharm.* 7 (2018) 9–16. <https://doi.org/10.1016/j.scp.2017.11.003>.

- 1202 [82] T. Masinga, M. Moyo, V.E. Pakade, Removal of hexavalent chromium by
1203 polyethyleneimine impregnated activated carbon: Intra-particle diffusion,
1204 kinetics and isotherms, *J. Mater. Res. Technol.* (2022).
1205 <https://doi.org/10.1016/j.jmrt.2022.03.062>.
- 1206 [83] A.H.M.G. Hyder, S.A. Begum, N.O. Egiebor, Adsorption isotherm and kinetic
1207 studies of hexavalent chromium removal from aqueous solution onto bone
1208 char, *J. Environ. Chem. Eng.* 3 (2015) 1329–1336.
1209 <https://doi.org/10.1016/j.jece.2014.12.005>.
- 1210 [84] K.S. Padmavathy, G. Madhu, P.V. Haseena, A study on Effects of pH,
1211 Adsorbent Dosage, Time, Initial Concentration and Adsorption Isotherm Study
1212 for the Removal of Hexavalent Chromium (Cr (VI)) from Wastewater by
1213 Magnetite Nanoparticles, *Procedia Technol.* 24 (2016) 585–594.
1214 <https://doi.org/10.1016/j.protcy.2016.05.127>.
- 1215 [85] J. Qu, Y. Wang, X. Tian, Z. Jiang, F. Deng, Y. Tao, Q. Jiang, KOH-activated
1216 porous biochar with high specific surface area for adsorptive removal of
1217 chromium (VI) and naphthalene from water: Affecting factors, mechanisms
1218 and reusability exploration, *J. Hazard. Mater.* 401 (2021) 123292.
1219 <https://doi.org/10.1016/j.jhazmat.2020.123292>.
- 1220 [86] U. Mahapatra, A.K. Manna, A. Chatterjee, A critical evaluation of conventional
1221 kinetic and isotherm modeling for adsorptive removal of hexavalent chromium
1222 and methylene blue by natural rubber sludge-derived activated carbon and
1223 commercial activated carbon, *Bioresour. Technol.* 343 (2022) 126135.
1224 <https://doi.org/10.1016/j.biortech.2021.126135>.
- 1225 [87] I. Langmuir, The adsorption of gases on plane surfaces of glass, mica and
1226 platinum., *J. Am. Chem. Soc.* 40 (1918) 1361–1403.
- 1227 [88] Mouhamadou et al., Investigation of Cr(VI) ions Adsorptive removal from
1228 aqueous solution onto TiO₂-AC composite: Non-linear equilibrium modelling
1229 and kinetics, *Int. J. Eng. Sci. Res. Technol.* 10 (2021) 41–54.
1230 <https://doi.org/https://doi.org/10.29121/ijesrt.v10.i1.2021.3>.
- 1231 [89] H.M.F. Freundlich, Over the adsorption in solution, *J. Phys. Chem.* 57 (1906)
1232 1100–1107.

- 1233 [90] I. Enniya, L. Rghioui, A. Jourani, Adsorption of hexavalent chromium in
1234 aqueous solution on activated carbon prepared from apple peels, *Sustain.*
1235 *Chem. Pharm.* 7 (2018) 9–16. <https://doi.org/10.1016/j.scp.2017.11.003>.
- 1236 [91] J. Wang, X. Guo, Adsorption isotherm models: Classification, physical
1237 meaning, application and solving method, *Chemosphere.* 258 (2020).
1238 <https://doi.org/10.1016/j.chemosphere.2020.127279>.
- 1239 [92] N. Ayawei, A.N. Ebelegi, D. Wankasi, Modelling and Interpretation of
1240 Adsorption Isotherms, 2017 (2017).
- 1241 [93] R. Saadi, Z. Saadi, R. Fazaeli, N.E. Fard, Monolayer and multilayer adsorption
1242 isotherm models for sorption from aqueous media, *Korean J. Chem. Eng.* 32
1243 (2015) 787–799. <https://doi.org/10.1007/s11814-015-0053-7>.
- 1244 [94] O. Hamdaoui, E. Naffrechoux, Modeling of adsorption isotherms of phenol and
1245 chlorophenols onto granular activated carbon. Part II. Models with more than
1246 two parameters, *J. Hazard. Mater.* 147 (2007) 401–411.
1247 <https://doi.org/10.1016/j.jhazmat.2007.01.023>.
- 1248 [95] S.O. Owalude, A.C. Tella, Removal of hexavalent chromium from aqueous
1249 solutions by adsorption on modified groundnut hull, *Beni-Suef Univ. J. Basic*
1250 *Appl. Sci.* 5 (2016) 377–388. <https://doi.org/10.1016/j.bjbas.2016.11.005>.
- 1251 [96] J.M. Barad, H.P. Kohli, M. Chakraborty, Adsorption of hexavalent chromium
1252 from aqueous stream by maghemite nanoparticles synthesized by the
1253 microemulsion method, *Energy Nexus.* 5 (2022) 100035.
1254 <https://doi.org/10.1016/j.nexus.2021.100035>.
- 1255 [97] S. Mortazavian, H. An, D. Chun, J. Moon, Activated carbon impregnated by
1256 zero-valent iron nanoparticles (AC / nZVI) optimized for simultaneous
1257 adsorption and reduction of aqueous hexavalent chromium : Material
1258 characterizations and kinetic studies, *Chem. Eng. J.* 353 (2018) 781–795.
1259 <https://doi.org/10.1016/j.cej.2018.07.170>.
- 1260 [98] T. Shahnaz, V. Sharma, S. Subbiah, S. Narayanasamy, Journal of Water
1261 Process Engineering Multivariate optimisation of Cr (VI), Co (III) and Cu (II)
1262 adsorption onto nanobentonite incorporated nanocellulose / chitosan aerogel
1263 using response surface methodology, *J. Water Process Eng.* 36 (2020)

- 1264 101283. <https://doi.org/10.1016/j.jwpe.2020.101283>.
- 1265 [99] M.C. Qhubu, B. Methula, T. Xaba, M. Moyo, V.E. Pakade, Iron-Zinc
1266 Impregnated Biochar Composite as a Promising Adsorbent for Toxic
1267 Hexavalent Chromium Remediation: Kinetics, Isotherms and Thermodynamics,
1268 Chem. Africa. (2021). <https://doi.org/10.1007/s42250-021-00273-5>.
- 1269 [100] M. De Luz-asunción, E.E. Pérez-ramírez, A.L. Martínez-hernández, V.M.
1270 Castano, V. Sánchez-mendieta, C. Velasco-santos, Chinese Journal of
1271 Chemical Engineering Non-linear modeling of kinetic and equilibrium data for
1272 the adsorption of hexavalent chromium by carbon nanomaterials : Dimension
1273 and functionalization, Chinese J. Chem. Eng. 27 (2019) 912–919.
1274 <https://doi.org/10.1016/j.cjche.2018.08.024>.
- 1275 [101] T.D. Ntuli, T.H. Mongwe, L.L. Sikeyi, O. Mkhari, N.J. Coville, E.N. Nxumalo, S.
1276 Maubane-nkadimeng, Environmental Nanotechnology , Monitoring &
1277 Management Removal of hexavalent chromium via an adsorption coupled
1278 reduction mechanism using olive oil derived carbon nano-onions, Environ.
1279 Nanotechnology, Monit. Manag. 16 (2021) 100477.
1280 <https://doi.org/10.1016/j.enmm.2021.100477>.
- 1281 [102] G. Pereira, R. Azevedo, J. Carlos, S. Soares, A. Barros, Synthesis and
1282 characterization of ZnO-Nb 2 O 5 catalysts for photodegradation of
1283 bromophenol blue, Catal. Today. 344 (2020) 240–246.
1284 <https://doi.org/10.1016/j.cattod.2019.04.059>.
- 1285 [103] N. Bouanimba, R. Zouaghi, N. Laid, T. Sehili, Factors in fl uencing the
1286 photocatalytic decolorization of Bromophenol blue in aqueous solution with
1287 different types of TiO 2 as photocatalysts, DES. 275 (2011) 224–230.
1288 <https://doi.org/10.1016/j.desal.2011.03.005>.
- 1289 [104] F. Harjati, P.W. Citradewi, G. Purwiandono, I. Fatimah, Green synthesis of
1290 hematite/TUD-1 nanocomposite as efficient photocatalyst for bromophenol blue
1291 and methyl violet degradation, Arab. J. Chem. 13 (2020) 8395–8410.
1292 <https://doi.org/10.1016/j.arabjc.2020.05.032>.
- 1293 [105] H.K. Paumo, S. Dalhatou, L.M. Katata-Seru, B.P. Kamdem, J.O. Tijani, V.
1294 Vishwanathan, A. Kane, I. Bahadur, TiO2 assisted photocatalysts for

- 1295 degradation of emerging organic pollutants in water and wastewater, *J. Mol.*
1296 *Liq.* 331 (2021) 115458. <https://doi.org/10.1016/j.molliq.2021.115458>.
- 1297 [106] Z.W. Heng, W.C. Chong, Y.L. Pang, L.C. Sim, H. Koo, Photocatalytic
1298 degradation of organic pollutants using green oil palm frond-derived carbon
1299 quantum dots/titanium dioxide as multifunctional photocatalysts under visible
1300 light radiation, *Chinese J. Chem. Eng.* (2021).
1301 <https://doi.org/10.1016/j.cjche.2021.10.021>.
- 1302 [107] H. Noreen, J. Iqbal, A. Arshad, R. Faryal, Ata-ur-Rahman, R. Khattak, Sunlight
1303 induced catalytic degradation of bromophenol blue and antibacterial
1304 performance of graphene nanoplatelets/polypyrrole nanocomposites, *J. Solid*
1305 *State Chem.* 275 (2019) 141–148. <https://doi.org/10.1016/j.jssc.2019.03.045>.
- 1306 [108] I. Fatimah, R. Nurillahi, I. Sahroni, O. Muraza, TiO₂-pillared saponite and
1307 photosensitization using a ruthenium complex for photocatalytic enhancement
1308 of the photodegradation of bromophenol blue, *Appl. Clay Sci.* 183 (2019)
1309 105302. <https://doi.org/10.1016/j.clay.2019.105302>.
- 1310 [109] H. Noreen, J. Iqbal, W. Hassan, G. Rahman, M. Yaseen, A.U. Rahman,
1311 Synthesis of graphene nanoplatelets/polythiophene nanocomposites With
1312 Enhanced Photocatalytic Degradation of Bromophenol Blue and Antibacterial
1313 Properties, *Mater. Res. Bull.* 142 (2021) 111435.
1314 <https://doi.org/10.1016/j.materresbull.2021.111435>.
- 1315 [110] G. Pereira da Costa, R.A. Rafael, J.C.S. Soares, A.B. Gaspar, Synthesis and
1316 characterization of ZnO-Nb₂O₅ catalysts for photodegradation of bromophenol
1317 blue, *Catal. Today.* 344 (2020) 240–246.
1318 <https://doi.org/10.1016/j.cattod.2019.04.059>.
- 1319 [111] R. Bouallouche, S. Dalhatou, A. Kane, N. Nasrallah, M. Hachemi, A. Amrane,
1320 A.A. Assadi, Reconsideration of the contribution of photogenerated ROS in
1321 methyl orange degradation on TiO₂, Cu₂O, WO₃, and Bi₂O₃ under low-
1322 intensity simulated solar light: mechanistic understanding of photocatalytic
1323 activity, *Euro-Mediterranean J. Environ. Integr.* 6 (2021) 1–10.
1324 <https://doi.org/10.1007/s41207-021-00276-1>.
- 1325 [112] S. Dalhatou, C. Pétrier, S. Laminsi, S. Baup, Sonochemical removal of

- 1326 naphthol blue black azo dye: influence of parameters and effect of mineral ions,
1327 Int. J. Environ. Sci. Technol. 12 (2015) 35–44. <https://doi.org/10.1007/s13762->
1328 013-0432-8.
- 1329 [113] L.N. Dlamini, R.W. Krause, G.U. Kulkarni, S.H. Durbach, Photodegradation of
1330 bromophenol blue with fluorinated TiO₂ composite, Appl. Water Sci. 1 (2011)
1331 19–24. <https://doi.org/10.1007/s13201-011-0004-3>.
- 1332 [114] G. Murugadoss, N. Kandhasamy, M. Rajesh Kumar, A.K. Alanazi, F. Khan, B.
1333 Salhi, H.M. Yadav, Role of the dopant (silver) inclusion on before and after core
1334 metal-oxide reaction: Application on textile dyes removal, Inorg. Chem.
1335 Commun. 137 (2022) 109186. <https://doi.org/10.1016/j.inoche.2021.109186>.
- 1336 [115] S. Sohrabi, F. Akhlaghian, Modeling and optimization of phenol degradation
1337 over copper-doped titanium dioxide photocatalyst using response surface
1338 methodology, Process Saf. Environ. Prot. 99 (2015) 120–128.
1339 <https://doi.org/10.1016/j.psep.2015.10.016>.
- 1340 [116] S. Sharafinia, A. Farrokhnia, E. Ghasemian, Colloids and Surfaces A :
1341 Physicochemical and Engineering Aspects The adsorption of cationic dye onto
1342 ACPMG @ ZIF-8 core-shell , optimization using central composite response
1343 surface methodology (CCRSM), Colloids Surfaces A Physicochem. Eng. Asp.
1344 634 (2022) 128039. <https://doi.org/10.1016/j.colsurfa.2021.128039>.
- 1345 [117] C. Cojocar, L. Clima, Polymer assisted ultrafiltration of AO7 anionic dye from
1346 aqueous solutions: Experimental design, multivariate optimization, and
1347 molecular docking insights, J. Memb. Sci. 604 (2020).
1348 <https://doi.org/10.1016/j.memsci.2020.118054>.
- 1349 [118] S. Sohrabi, F. Akhlaghian, Modeling and optimization of phenol degradation
1350 over copper-doped titanium dioxide photocatalyst using response surface
1351 methodology, Process Saf. Environ. Prot. 99 (2016) 120–128.
1352 <https://doi.org/10.1016/j.psep.2015.10.016>.
- 1353 [119] J. Zhang, D. Fu, Y. Xu, C. Liu, Optimization of parameters on photocatalytic
1354 degradation of chloramphenicol using TiO₂ as photocatalyst by response
1355 surface methodology, J. Environ. Sci. 22 (2010) 1281–1289.
1356 [https://doi.org/10.1016/S1001-0742\(09\)60251-5](https://doi.org/10.1016/S1001-0742(09)60251-5).

- 1357 [120] H. Noreen, J. Iqbal, A. Arshad, R. Faryal, Ata-ur-Rahman, R. Khattak, Sunlight
1358 induced catalytic degradation of bromophenol blue and antibacterial
1359 performance of graphene nanoplatelets/polypyrrole nanocomposites, J. Solid
1360 State Chem. 275 (2019) 141–148. <https://doi.org/10.1016/j.jssc.2019.03.045>.
- 1361 [121] I. Fatimah, E. Zunita Pratiwi, W. Prio Wicaksono, Synthesis of magnetic
1362 nanoparticles using Parkia speciosa Hassk pod extract and photocatalytic
1363 activity for Bromophenol blue degradation, Egypt. J. Aquat. Res. 46 (2020) 35–
1364 40. <https://doi.org/10.1016/j.ejar.2020.01.001>.



Revised Graphical
abstract_S0.1.docx

1365

Graphical abstrat

